Dynamical Structure and Evolution of Stellar Systems

Ven, Glenn van de

Citation

Ven, G. van de. (2005, December 1). *Dynamical Structure and Evolution of Stellar Systems*. Retrieved from https://hdl.handle.net/1887/3740

CHAPTER 2

THE DYNAMICAL DISTANCE AND INTRINSIC STRUCTURE OF THE GLOBULAR CLUSTER ω CENTAURI

ABSTRACT

We determine the dynamical distance D, inclination i, mass-to-light ratio M/L and the intrinsic orbital structure of the globular cluster ω Cen, by fitting axisymmetric dynamical models to the ground-based proper motions of van Leeuwen et al. (2000) and line-of-sight velocities from four independent data-sets. We bring the kinematic measurements onto a common coordinate system, and select on cluster membership and on measurement error. This provides a homogeneous data-set of 2295 stars with proper motions accurate to $0.20\,\mathrm{mas\,yr^{-1}}$ and 2163 stars with line-of-sight velocities accurate to $2\,\mathrm{km\,s^{-1}}$, out to about half the tidal radius.

We correct the observed velocities for perspective rotation caused by the space motion of the cluster, and show that the residual solid-body rotation component in the proper motions (caused by relative rotation of the photographic plates from which they were derived) can be taken out without any modeling other than assuming axisymmetry. This also provides a tight constraint on $D \tan i$. The corrected mean velocity fields are consistent with regular rotation, and the velocity dispersion fields display significant deviations from isotropy.

We model ω Cen with an axisymmetric implementation of Schwarzschild's orbit superposition method, which accurately fits the surface brightness distribution, makes no assumptions about the degree of velocity anisotropy in the cluster, and allows for radial variations in M/L. We bin the individual measurements on the plane of the sky to search efficiently through the parameter space of the models. Tests on an analytic model demonstrate that this approach is capable of measuring the cluster distance to an accuracy of about 6 per cent. Application to ω Cen reveals no dynamical evidence for a significant radial dependence of M/L, in harmony with the relatively long relaxation time of the cluster. The best-fit dynamical model has a stellar V-band mass-to-light ratio $M/L_V = 2.5 \pm 0.1\ \mathrm{M_\odot/L_\odot}$ and an inclination $i = 50° \pm 4°$, which corresponds to an average intrinsic axial ratio of 0.78 ± 0.03. The best-fit dynamical distance $D = 4.8 \pm 0.3$ kpc (distance modulus 13.75 ± 0.13 mag) is significantly larger than obtained by means of simple spherical or constant-anisotropy axisymmetric dynamical models, and is consistent with the canonical value 5.0 ± 0.2 kpc obtained by photometric methods. The total mass of the cluster is $(2.5 \pm 0.3) \times 10^6\ \mathrm{M_\odot}$.

The best-fit model is close to isotropic inside a radius of about 10 arcmin and becomes increasingly tangentially anisotropic in the outer region, which displays significant mean rotation. This phase-space structure may well be caused by the effects of the tidal field of the Milky Way. The cluster contains a separate disk-like component in the radial range between 1 and 3 arcmin, contributing about 4% to the total mass.

G. van de Ven, R.C.E. van den Bosch, E.K. Verolme, P.T. de Zeeuw

1   INTRODUCTION

THE globular cluster ω Cen (NGC 5139) is a unique window into astrophysics (van Leeuwen, Hughes & Piotto 2002). It is the most massive globular cluster of our Galaxy, with an estimated mass between $2.4 \times 10^6 M_\odot$ (Mandushev, Staneva & Spasova 1991) and $5.1 \times 10^6 M_\odot$ (Meylan et al. 1995). It is also one of the most flattened globular clusters in the Galaxy (e.g., Geyer, Nelles & Hopp 1983) and it shows clear differential rotation in the line-of-sight (Merritt, Meylan & Mayor 1997). Furthermore, multiple stellar populations can be identified (e.g., Freeman & Rodgers 1975; Lee et al. 1999; Pancino et al. 2000; Bedin et al. 2004). Since this is unusual for a globular cluster, a whole range of different formation scenarios of ω Cen have been suggested, from self-enrichment in an isolated cluster or in the nucleus of a tidally stripped dwarf galaxy, to a merger between two or more globular clusters (e.g., Icke & Alcaino 1988; Freeman 1993; Lee et al. 2002; Tsuchiya, Korchagin & Dinescu 2004).

ω Cen has a core radius of $r_c = 2.6$ arcmin, a half-light (or effective) radius of $r_h = 4.8$ arcmin and a tidal radius of $r_t = 45$ arcmin (e.g., Trager, King & Djorgovski 1995). The resulting concentration index $\log(r_t/r_c) \sim 1.24$ implies that ω Cen is relatively loosely bound. In combination with its relatively small heliocentric distance of 5.0 ± 0.2 kpc (Harris 1996)[1]. This makes it is possible to observe individual stars over almost the entire extent of the cluster, including the central parts. Indeed, line-of-sight velocity measurements[2] have been obtained for many thousands of stars in the field of ω Cen (Suntzeff & Kraft 1996, hereafter SK96; Mayor et al. 1997, hereafter M97; Reijns et al. 2005, hereafter Paper II; Xie, Gebhardt et al. in preparation, hereafter XGEA). Recently, also high-quality measurements of proper motions of many thousands of stars in ω Cen have become available, based on ground-based photographic plate observations (van Leeuwen et al. 2000, hereafter Paper I) and Hubble Space Telescope (HST) imaging (King & Anderson 2002).

The combination of proper motions with line-of-sight velocity measurements allows us to obtain a dynamical estimate of the distance to ω Cen and study its internal dynamical structure. While line-of-sight velocity observations are in units of $\mathrm{km\,s^{-1}}$, proper motions are angular velocities and have units of (milli)arcsec yr^{-1}. A value for the distance is required to convert these angular velocities to $\mathrm{km\,s^{-1}}$. Once this is done, the proper motion and line-of-sight velocity measurements can be combined into a three-dimensional space velocity, which can be compared to kinematic observables that are predicted by dynamical models. By varying the input parameters of these models, the set of model parameters (including the distance) that provides the best-fit to the observations can be obtained. Similar studies for other globular clusters, based on comparing modest numbers of line-of-sight velocity and proper motion measurements with simple spherical dynamical models, were published for M3 (Cudworth 1979), M22 (Peterson & Cudworth 1994), M4 (Peterson, Rees & Cudworth 1995; see also Rees 1997), and M15 (McNamara, Harrison & Baumgardt 2004).

A number of dynamical models which reproduce the line-of-sight velocity measurements have been published. As no proper motion information was included in these models, the distance could not be fitted and had to be assumed. Furthermore, all

---

[1] Throughout this chapter we use this distance of 5.0 ± 0.2 kpc, obtained with photometric methods, as the canonical distance.

[2] Instead of the often-used term *radial* velocities, we adopt the term *line-of-sight* velocities, to avoid confusion with the decomposition of the proper motions in the plane of the sky into a radial and tangential component.

these models were limited by the flexibility of the adopted techniques and assumed either spherical geometry (Meylan 1987, Meylan et al. 1995) or an isotropic velocity distribution (Merritt et al. 1997). Neither of these assumptions is true for ω Cen (Geyer et al. 1983; Merrifield & Kent 1990). Recent work, using an axisymmetric implementation of Schwarzschild's (1979) orbit superposition method, shows that it is possible to fit anisotropic dynamical models to (line-of-sight) kinematic observations of non-spherical galaxies (van der Marel et al. 1998; Cretton et al. 1999; Cappellari et al. 2002; Verolme et al. 2002; Gebhardt et al. 2003; Krajnović et al. 2005). Here, we extend Schwarzschild's method in such a way that it can deal with a combination of proper motion and line-of-sight velocity measurements of individual stars. This allows us to derive an accurate dynamical distance and to improve our understanding of the internal structure of ω Cen.

It is possible to incorporate the discrete kinematic measurements of ω Cen directly in dynamical models by using maximum likelihood techniques (Merritt & Saha 1993; Merritt 1993; Merritt 1997; Romanowsky & Kochanek 2001; Kleyna et al. 2002), but these methods are non-linear, are not guaranteed to find the global best-fitting model, and are very CPU-intensive for data-sets consisting of several thousands of measurements. We therefore decided to bin the measurements instead and obtain the velocity moments in a set of apertures on the plane of the sky. While this method is (in principle) slightly less accurate, as some information in the data may be lost during the binning process, it is much faster, which allows us to make a thorough investigation of the parameter space of ω Cen in a relatively short time. It should also give a good starting point for a subsequent maximum likelihood model using the individual measurements.

This chapter is organized as follows. In Section 2, we describe the proper motion and line-of-sight velocity measurements and transform them to a common coordinate system. The selection of the kinematic measurements on membership and measurement error is outlined in Section 3. In Section 4, we correct the kinematic measurements for perspective rotation and show that a residual solid-body rotation component in the proper motions can be taken out without any modeling other than assuming axisymmetry. This also provides a tight constraint on the inclination of the cluster. In Section 5, we describe our axisymmetric dynamical modeling method, and test it in Section 6 on an analytical model. In Section 7, we construct the mass model for ω Cen, bin the individual kinematic measurements on the plane of the sky and describe the construction of dynamical models that we fit to these observations. The resulting best-fit parameters for ω Cen are presented in Section 8. We discuss the intrinsic structure of the best-fit model in Section 9, and draw our conclusions in Section 10.

2   OBSERVATIONS

We briefly describe the stellar proper motion and line-of-sight velocity observations of ω Cen that we use to constrain our dynamical models (see Table 1). We then align and transform them to a common coordinate system.

2.1   PROPER MOTIONS

The proper motion study in Paper I is based on 100 photographic plates of ω Cen, obtained with the Yale-Columbia 66 cm refractor telescope. The first-epoch observations were taken between 1931 and 1935, for a variable star survey of ω Cen (Martin

Source	Extent (arcmin)	Observed (#stars)	Selected (#stars)	Precision (km s^{-1})
proper motions				
Paper I	0–30	9847	2295	< 4.7
line-of-sight velocities				
SK96	3–23	360	345	2.2
M97	0–22	471	471	0.6
Paper II	0–38	1966	1588	2.0
XGEA	0–3	4916	1352	1.1
Merged	0–30		2163	< 2.0

TABLE 1 — *Overview of the proper motions and line-of-sight velocity data-sets for ω Cen. The last row describes the four different line-of-sight velocity data-sets merged together, using the stars in common. The precision is estimated as the median of the (asymmetric) velocity error distribution. If a selection on the velocity errors is applied (§ 3), the upper limit is given. For the proper motions, we assume a canonical distance of 5 kpc to convert from mas yr^{-1} to km s^{-1}.*

1938). Second-epoch plates, specifically meant for the proper motion study, were taken between 1978 and 1983. The plates from both periods were compared and proper motions were measured for 9847 stars. The observations cover a radial range of about 30 arcmin from the cluster center.

2.2 LINE-OF-SIGHT VELOCITIES

We use line-of-sight velocity observations from four different data-sets: the first two, by SK96 and M97, from the literature, the third is described in the companion Paper II and the fourth (XGEA) was provided by Karl Gebhardt in advance of publication.

SK96 used the ARGUS multi-object spectrograph on the CTIO 4 m Blanco telescope to measure, from the Ca II triplet range of the spectrum, the line-of-sight velocities of bright giant and subgiant stars in the field of ω Cen. They found respectively 144 and 199 line-of-sight velocity members, and extended the bright sample to 161 with measurements by Patrick Seitzer. The bright giants cover a radial range from 3 to 22 arcmin, whereas the subgiants vary in distance between 8 and 23 arcmin. From the total data-set of 360 stars, we remove the 6 stars without (positive) velocity error measurement together with the 9 stars for which we do not have a position (see § 2.3.1), leaving a total of 345 stars.

M97 published 471 high-quality line-of-sight velocity measurements of giants in ω Cen, taken with the photoelectric spectrometer CORAVEL, mounted on the 1.5 m Danish telescope at Cerro La Silla. The stars in their sample are located between 10 arcsec and 22 arcmin from the cluster center.

In Paper II, we describe the line-of-sight velocity measurements of 1966 individual stars in the field of ω Cen, going out to about 38 arcmin. Like SK96, we observed with ARGUS, but used the Mg*b* wavelength range. We use the 1589 cluster members, but exclude the single star for which no positive velocity error measurement is available.

Finally, the data-set of XGEA contains the line-of-sight velocities of 4916 stars in the central 3 arcmin of ω Cen. These measurements were obtained in three epochs over a time span of four years, using the Rutgers Imaging Fabry-Perot Spectrophotometer on the CTIO 1.5 m telescope. During the reduction process, some slightly

smeared out single stars were accidentally identified as two fainter stars. Also, contaminating light from surrounding stars can lead to offsets in the line-of-sight velocity measurements. To exclude (most of) these misidentifications (Gebhardt, priv. comm.), we select the 1352 stars with a measured (R-band) magnitude brighter than 14.5.

2.3 COORDINATE SYSTEM: POSITIONS

We constrain our dynamical models by merging all the above data-sets. We convert all stellar positions to the same projected Cartesian coordinates and align the different data-sets with respect to each other by matching the stars in common between the different data-sets. Next, we rotate the coordinates over the observed position angle of ω Cen to align with its major and minor axis, and give the relation with the intrinsic axisymmetric coordinate system we assume for our models.

2.3.1 Projected Cartesian coordinates (x'', y'')

The stellar positions in Paper I are given in equatorial coordinates α and δ (in units of degrees for J2000), with the cluster center at $\alpha_0 = 201°69065$ and $\delta_0 = -47°47855$. For objects with small apparent sizes, these equatorial coordinates can be converted to Cartesian coordinates by setting $x'' = -\Delta\alpha \cos\delta$ and $y'' = \Delta\delta$, with x'' in the direction of West and y'' in the direction of North, and $\Delta\alpha \equiv \alpha - \alpha_0$ and $\Delta\delta \equiv \delta - \delta_0$. However, this transformation results in severe projection effects for objects that have a large angular diameter or are located at a large distance from the equatorial plane. Since both conditions are true for ω Cen, we must project the coordinates of each star on the plane of the sky along the line-of-sight vector through the cluster center

$$
\begin{aligned}
x'' &= -r_0 \cos\delta \sin\Delta\alpha, \\
y'' &= r_0 \left(\sin\delta \cos\delta_0 - \cos\delta \sin\delta_0 \cos\Delta\alpha\right),
\end{aligned}
\tag{2.1}
$$

with scaling factor $r_0 \equiv 10800/\pi$ to have x'' and y'' in units of arcmin. The cluster center is at $(x'', y'') = (0, 0)$.

The stellar observations by SK96 are tabulated as a function of the projected radius to the center only. However, for each star for which its ROA number (Woolley 1966) appears in the Tables of Paper I or M97, we can reconstruct the positions from these data-sets. In this way, only nine stars are left without a position. The positions of the stars in the M97 data-set are given in terms of the projected polar radius R'' in arcsec from the cluster center and the projected polar angle θ'' in radians from North to East, and can be straightforwardly converted into Cartesian coordinates x'' and y''. For Paper II, we use the Leiden Identification (LID) number of each star, to obtain the stellar positions from Paper I. The stellar positions in the XGEA data-set are already in the required Cartesian coordinates x'' and y''.

2.3.2 Alignment between data-sets

Although for all data-sets the stellar positions are now in terms of the projected Cartesian coordinates (x'', y''), (small) misalignments between the different data-sets are still present. These misalignments can be eliminated using the stars in common between the different data-sets. As the data-set of Paper I covers ω Cen fairly uniformly over much of its extent, we take their stellar positions as a reference frame.

All the positions for the Paper II data-set and most of the positions for the SK96 data-set come directly from Paper I, and hence are already aligned. For the M97 and

XGEA data-set, we use the `DAOMASTER` program (Stetson 1992), to obtain the transformation (horizontal and vertical shift plus rotation) that minimizes the positional difference between the stars that are in common with those in Paper I: 451 for the M97 data-set and 1667 for the XGEA data-set.

2.3.3   Major-minor axis coordinates (x', y')

With all the data-sets aligned, we finally convert the stellar positions into the Cartesian coordinates (x', y'), with the x'-axis and y'-axis aligned with respectively the observed major and minor axis of ω Cen. Therefore we have to rotate (x'', y'') over the position angle of the cluster. This angle is defined in the usual way as the angle between the observed major axis and North (measured counterclockwise through East).

To determine the position angle, we fit elliptic isophotes to the smoothed Digital Sky Survey (`DSS`) image of ω Cen, while keeping the center fixed. In this way, we find a nearly constant position angle of $100°$ between 5 and 15 arcmin from the center of the cluster. This is consistent with an estimate by Seitzer (priv. comm.) from a U-band image, close to the value of $96°$ found by White & Shawl (1987), but significantly larger than the position angle of $91.3°$ measured in Paper I from star counts.

2.3.4   Intrinsic axisymmetric coordinates (x, y, z)

Now that we have aligned the coordinates in the plane of the sky (x', y') with the observed major and the major axis, the definition of the intrinsic coordinate system of our models and the relation between both becomes straightforward. We assume the cluster to be axisymmetric and express the intrinsic properties of the model in terms of Cartesian coordinates (x, y, z), with the z-axis the symmetry axis. The relation between the intrinsic and projected coordinates is then given by

$$\begin{aligned} x' &= y, \\ y' &= -x\cos i + z\sin i, \\ z' &= -x\sin i - z\cos i. \end{aligned} \tag{2.2}$$

The z'-axis is along the line-of-sight in the direction away from us[3], and i is the inclination along which the object is observed, from $i = 0°$ face-on to $i = 90°$ edge-on.

2.4   COORDINATE SYSTEM: VELOCITIES

After the stellar positions have been transformed to a common coordinate system, we also convert the proper motions and line-of-sight velocities to the same (three-dimensional) Cartesian coordinate system. We center it around zero (mean) velocity by subtracting the systemic velocity in all three directions, and relate it to the intrinsic axisymmetric coordinate system.

2.4.1   Proper motions

The proper motions (in $mas\,yr^{-1}$) of Paper I are given in the directions East and North, i.e., in the direction of $-x''$ and y'' respectively. After rotation over the position angle of $100°$, we obtain the proper motion components $\mu_{x'}$ and $\mu_{y'}$, aligned with the observed major and minor axis of ω Cen, and similarly, for the proper motion errors.

---

[3]In the common (mathematical) definition of a Cartesian coordinate system the z'-axis would point towards us, but here we adopt the astronomical convention to have positive line-of-sight away from us.

2.4.2 Multiple line-of-sight velocity measurements

In Paper II, the measured line-of-sight velocities are compared with those of SK96 and M97 for the stars in common. A systematic offset in velocity between the different data-sets is clearly visible in Fig. 1 of that paper. We measure this offset with respect to the M97 data-set, since it has the highest velocity precision and more than a hundred stars in common with the other three data-sets: 129 with SK96, 312 with Paper II[4] and 116 with XGEA. As in Paper II, we apply four-sigma clipping, i.e., we exclude all stars for which the measured velocities differ by more than four times the combined velocity error. This leaves respectively 117, 284 and 109 stars in common between M97 and the three data-sets of SK96, Paper II and XGEA. The (weighted[5]) mean velocity offsets of the data-set of M97 minus the three data-sets of SK96, Paper II and XGEA, are respectively -0.41 ± 0.08 km s^{-1}, 1.45 ± 0.07 km s^{-1} and 0.00 ± 0.12 km s^{-1}. For each of the latter three data-sets, we add these offsets to all observed line-of-sight velocities.

Next, for each star that is present in more than one data-set, we combine the multiple line-of-sight velocity measurements. Due to non-overlapping radial coverage of the data-set of SK96 and XGEA, there are no stars in common between these two data-sets, and hence no stars that appear in all four data-sets. There are 138 stars with position in common between three data-sets and 386 stars in common between two data-sets.

For the 138 stars in common between three data-sets, we check if the three pairwise velocity differences satisfy the four-sigma clipping criterion. For 6 stars, we find that two of the three pairs satisfy the criterion, and we select the two velocities that are closest to each other. For 7 stars, we only find a single pair that satisfies the criterion, and we select the corresponding two velocities. Similarly, we find for the 386 stars in common between two data-sets, 13 stars for which the velocity difference does not satisfy the criterion, and we choose the measurement with the smallest error. This means from the 524 stars with multiple velocity measurements, for 26 stars (5%) one of the measurements is removed as an outlier. This can be due to a chance combination of large errors, a misidentification or a binary; Mayor et al. (1996) estimated the global frequency of short-period binary systems in ω Cen to be 3–4%.

As pointed out in § 2.6 of Paper II, we can use for the stars in common between (at least) three data-sets, the dispersion of the pairwise differences to calculate the external (instrumental) dispersion for each of the data-sets. In this way, we found in Paper II that the errors tabulated in SK96 are under-estimated by about 40% and hence increased them by this amount, whereas those in M97 are well-calibrated. Unfortunately, there are too few stars in common with the XGEA data-set for a similar (statistically reliable) external error estimate.

In the final sample, we have 125 stars with the weighted mean of three velocity measurements and 373 stars with the weighted mean of two velocity measurements. Together with the 2596 single velocity measurements, this gives a total of 3094 cluster stars with line-of-sight velocities.

---

[4]In Paper II, we report only 267 stars in common with the data-set of M97. The reason is that there the comparison is based on matching ROA numbers, and since not all stars from Paper II have a ROA number, we find here more stars in common by matching in position.

[5]To calculate the mean and dispersion of a sample, we use the weighted estimators and corresponding uncertainties as described in Appendix A of Paper II.

2.4.3 Systemic velocities

To center the Cartesian velocity system around zero mean velocity, we subtract from both the proper motion data-sets and the merged line-of-sight data-set the (remaining) systemic velocities. In combination with the cluster proper motion values from Table 4 of Paper I, we find the following systemic velocities

$$
\begin{aligned}
\mu_{x'}^{\mathrm{sys}} &= 3.88 \pm 0.41 \quad \mathrm{mas\,yr^{-1}}, \\
\mu_{y'}^{\mathrm{sys}} &= -4.44 \pm 0.41 \quad \mathrm{mas\,yr^{-1}}, \\
v_{z'}^{\mathrm{sys}} &= 232.02 \pm 0.03 \quad \mathrm{km\,s^{-1}}.
\end{aligned}
\tag{2.3}
$$

2.4.4 Intrinsic axisymmetric coordinate system

In our models, we calculate the velocities in units of $\mathrm{km\,s^{-1}}$. If we assume a distance D (in units of kpc), the conversion of the proper motions in units of $\mathrm{mas\,yr^{-1}}$ into units of $\mathrm{km\,s^{-1}}$ is given by

$$
v_{x'} = 4.74\,D\,\mu_{x'} \quad \text{and} \quad v_{y'} = 4.74\,D\,\mu_{y'}.
\tag{2.4}
$$

The relation between observed $(v_{x'}, v_{y'}, v_{x'})$ and intrinsic (v_x, v_y, v_z) velocities is the same as in eq. (2.2), with the coordinates replaced by the corresponding velocities.

In addition to Cartesian coordinates, we also describe the intrinsic properties of our axisymmetric models in terms of the usual cylindrical coordinates (R, ϕ, z), with $x = R\cos\phi$ and $y = R\sin\phi$. In these coordinates the relation between the observed and intrinsic velocities is

$$
\begin{aligned}
v_{x'} &= v_R \sin\phi + v_\phi \cos\phi, \\
v_{y'} &= (-v_R \cos\phi + v_\phi \sin\phi)\cos i + v_z \sin i, \\
v_{z'} &= (-v_R \cos\phi + v_\phi \sin\phi)\sin i + v_z \cos i.
\end{aligned}
\tag{2.5}
$$

3 SELECTION

We discuss the selection of the cluster members from the different data-sets, as well as some further removal of stars that cause systematic deviations in the kinematics.

3.1 PROPER MOTIONS

In Paper I, a membership probability was assigned to each star. We use the stars for which we also have line-of-sight velocity measurements to investigate the membership determination. Furthermore, in Paper I the image of each star was inspected and classified according to its separation from other stars. We study the effect of the disturbance by a neighboring star on the kinematics. Finally, after selection of the undisturbed cluster members, we exclude the stars with relatively large uncertainties in their proper motion measurements, which cause a systematic overestimation of the mean proper motion dispersion.

3.1.1 Membership determination

The membership probability in Paper I was assigned to each star in the field by assuming that the distribution of stellar velocities is Gaussian. In most studies, this is done by adopting one common distribution for the entire cluster. However, this does not take into account that the internal dispersion, as well as the relative number

of cluster stars decreases with radius. To better incorporate these two effects, the membership probability in Paper I was calculated along concentric rings.

By matching the identification numbers and the positions of stars, we find that there are 3762 stars for which both proper motions and line-of-sight velocities are measured. This allows us to investigate the quality of the membership probability assigned in Paper I, as the separation of cluster and field stars is very clean in line-of-sight velocities (see e.g. Paper II, Fig. 4).

From the line-of-sight velocities, we find that of the 3762 matched stars, 3385 are cluster members. Indeed, most of these cluster stars, 3204 (95%), have a membership probability based on their proper motions of at least 68 per cent. Based on the latter criterion, the remaining 181 (5%) cluster stars are wrongly classified as field stars in Paper I. From the 3762 matched stars, 377 stars are field stars from the line-of-sight velocity data-set of Paper II. Based on a membership probability of 68 per cent, 54 (14%) of these field stars are wrongly classified as cluster members in Paper I. This fraction of field stars misclassified as cluster stars is an upper limit, since the obvious field stars are already removed from the proper motion data-set of Paper I.

Wrongly classifying cluster stars as field stars is relatively harmless for our purpose, since it only reduces the total cluster data-set. However, classifying field stars as members of the cluster introduces stars from a different population with different (kinematical) properties. With a membership probability of 99.7 per cent the fraction of field stars misclassified as cluster stars reduces to 5%. However, at the same time we expect to miss almost 30% of the cluster stars as they are wrongly classified as field stars. Taking also into account that the additional selections on disturbance by neighboring stars and velocity error below remove (part of) the field stars misclassified as cluster stars, we consider stars with a membership probability of at least 68 per cent as cluster members.

While for the 3762 matched stars, the line-of-sight velocities confirm 3385 stars as cluster members, from the remaining 6084 (unmatched) stars of Paper I, 4597 stars have a proper motion membership probability of at least 68 per cent. From the resulting proper motion distribution, we remove 83 outliers with proper motions five times the standard deviation away from the mean, leaving a total of 7899 cluster stars.

3.1.2 *Disturbance by neighboring stars*

In Paper I, each star was classified according to its separation from other stars on a scale from 0 to 4, from completely free to badly disturbed by a neighboring star. In Fig. 1, we show the effect of the disturbance on the proper motion dispersion. The (smoothed) profiles are constructed by calculating the mean proper motion dispersion of the stars binned in concentric rings, taking the individual measurement errors into account (Appendix A). The proper motions in the x'-direction give rise to the velocity dispersion profiles $\sigma_{x'}$ in the left panel. The proper motions in the y'-direction yield the dispersion profiles $\sigma_{y'}$ in the right panel. The thickest curves are the dispersion profiles for all 7899 cluster stars with proper motion measurements. The other curves show how, especially in the crowded center of ω Cen, the dispersion decreases significantly when sequentially stars of class 4 (severely disturbed) to class 1 (slightly disturbed) are removed. We select the 4415 undisturbed stars of class 0.

The membership determination is cleaner for undisturbed stars, so that above fraction of 5% of the cluster stars misclassified as field stars becomes smaller than 3% if only stars of class 0 are selected. The dispersion profiles $\sigma_{x'}$ and $\sigma_{y'}$ in Fig. 1
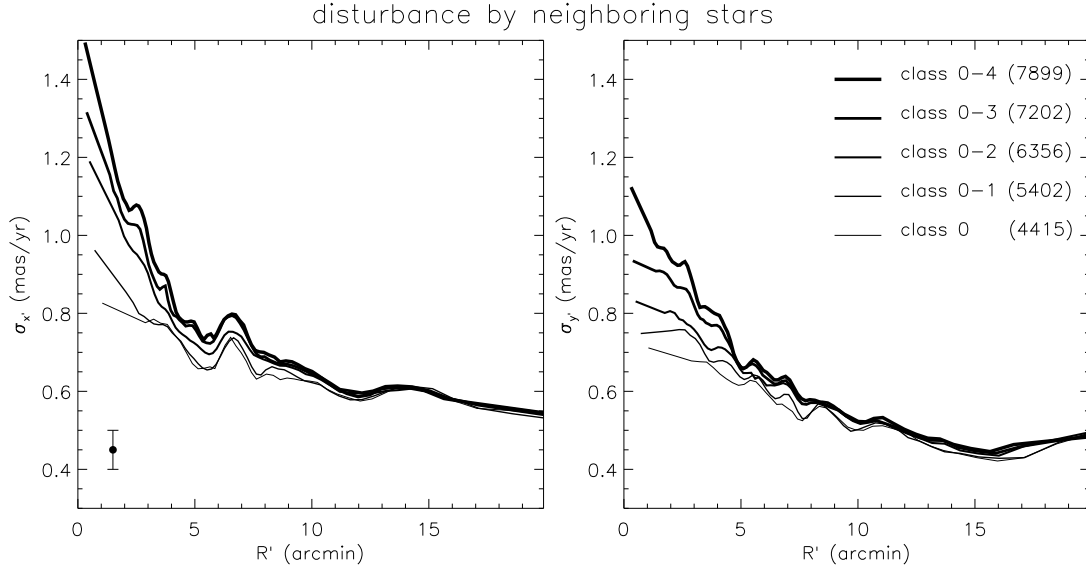
FIGURE 1 — *Velocity dispersion profiles, calculated along concentric rings, from the proper motions of Paper I. The dispersion profiles from the proper motions in the x'-direction (y'-direction) are shown in the left (right). The error bar at the bottom-left indicates the typical uncertainty in the velocity dispersion. The thickest curves are the dispersion profiles for all 7899 cluster stars with proper motion measurements. The other curves show how the dispersion decreases significantly, especially in the crowded center of ω Cen, when sequentially stars of class 4 (severely disturbed) to class 1 (slightly disturbed) are removed. We select the 4415 undisturbed stars of class 0.*

are systematically offset with respect to each other, demonstrating that the velocity distribution in ω Cen is anisotropic. We discuss this further in § 4.6 and § 9.2.

3.1.3 Selection on proper motion error

After selection of the cluster members that are not disturbed by neighboring stars, it is likely that the sample of 4415 stars still includes (remaining) interlopers and stars with uncertain proper motion measurements, which can lead to systematic deviations in the kinematics. Fig. 2 shows that the proper motion dispersion profiles decrease if we sequentially select a smaller number of stars by setting a tighter limit on the allowed error in their proper motion measurements.

Since the proper motion errors are larger for the fainter stars (see also Fig. 11 of Paper I), a similar effect happens if we select on magnitude instead. The decrease in dispersion is most prominent at larger radii as the above selection on disturbance by a neighboring star already removed the uncertain proper motion measurements in the crowded center of ω Cen. All dispersion profiles in the above are corrected for the broadening due to the individual proper motion errors (cf. Appendix A). The effect of this broadening, indicated by the dotted curve, is less than the decrease in the dispersion profiles due to the selection on proper motion error.

Since the kinematics do not change anymore significantly for a limit on the proper motion errors lower than 0.20 $\mathrm{mas\,yr^{-1}}$, we select the 2295 stars with proper motion errors below this limit. The preliminary HST proper motions of King & Anderson
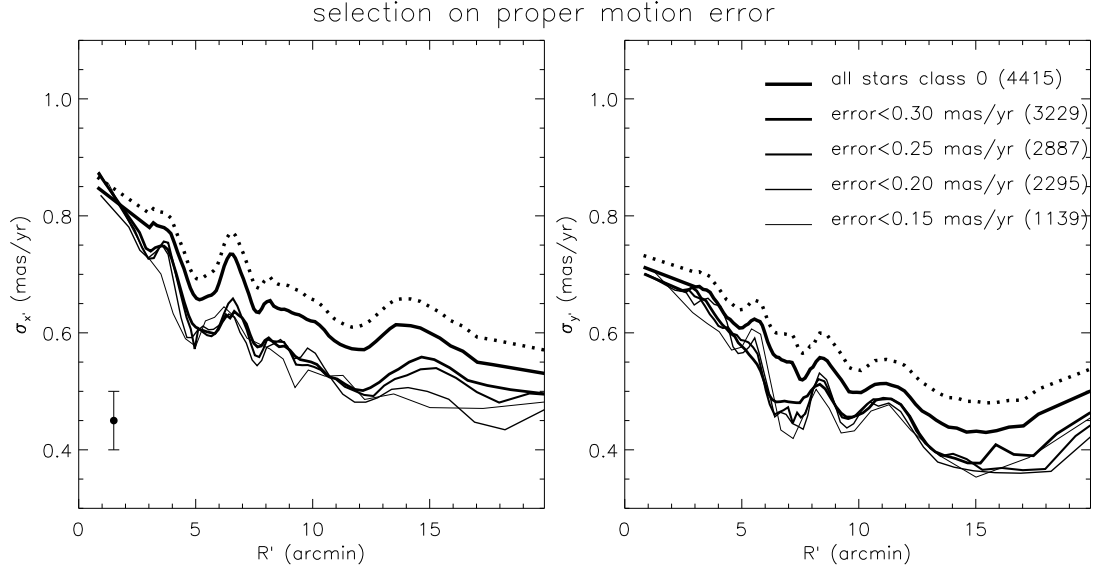
selection on proper motion error

FIGURE 2 — *Proper motion dispersion profiles as in Fig. 1. Starting with all undisturbed (class 0) cluster stars (thickest solid curve), sequentially a smaller number of stars is selected by setting a tighter limit on the allowed error in their proper motion measurements. The dispersion decreases if the stars with uncertain proper motion measurements are excluded. This effect is significant and larger than the dispersion broadening due to the individual velocity errors, indicated by the dotted curve. We select the 2295 stars with proper motion error smaller than 0.20 mas yr^{-1}, since below this limit the kinematics stay similar.*

(2002) in the center of ω Cen ($R' \sim 1$ arcmin) give rise to mean proper motion dispersion $\sigma_{x'} = 0.81 \pm 0.08$ mas yr^{-1} and $\sigma_{y'} = 0.77 \pm 0.08$ mas yr^{-1}, depending on the magnitude cut-off. In their outer calibration field ($R' \sim 14$ arcmin), the average dispersion is about 0.41 ± 0.03 mas yr^{-1}. These values are consistent with the mean proper motion dispersion of the 2295 selected stars at those radii. We are therefore confident that the proper motion kinematics have converged.

The spatial distribution of the selected stars is shown in the left panel of Fig. 4. In the two upper panels of Fig. 5, the distributions of the two proper motion components (left panels) and the corresponding errors (right panels) of the $N_{\rm sel} = 2295$ selected stars are shown as shaded histograms, on top of the histograms of the $N_{\rm mem} = 7899$ cluster members. The selection removes the extended tails, making the distribution narrower with an approximately Gaussian shape.

3.2 LINE-OF-SIGHT VELOCITIES

For each of the four different line-of-sight velocity data-sets separately, the velocity dispersion profiles of the selected (cluster) stars (§ 2.2 and Table 1) are shown in Fig. 3. The dotted curve is the dispersion profile of all the 4916 stars observed by XGEA, whereas the dotted-dashed curve is based on the 1352 selected stars with a measured magnitude brighter than 14.5, showing that fainter misidentified stars lead to an under-estimation of the line-of-sight velocity dispersion. Although the dispersion profile of the M97 data-set (long dashed curve) seems to be systematically higher than those of the other data-sets, it is based on a relatively small number of
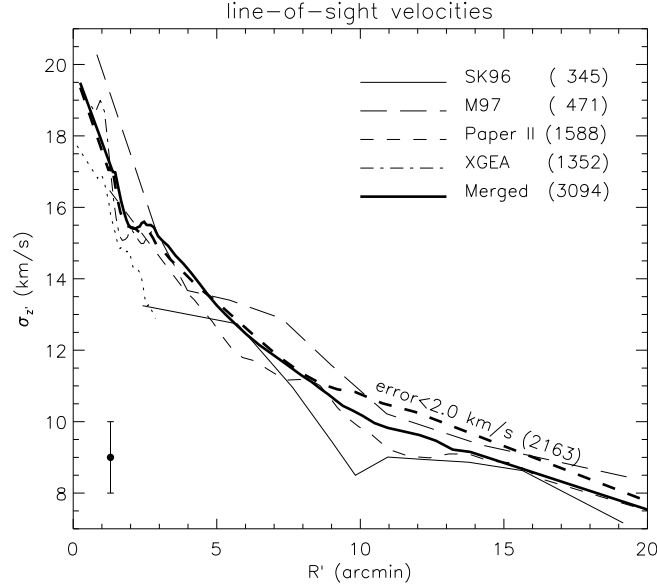
FIGURE 3 — *Velocity dispersion profiles, calculated along concentric rings, for the four different line-of-sight velocity data-sets separately and after they have been merged. The dotted curve shows the under-estimated dispersion for the XGEA data-set if also the faint stars are included. From the merged data-set of 3094 stars we select the 2163 stars with line-of-sight velocity errors smaller than 2.0 km s^{-1}, resulting in a dispersion profile (thick dashed curve) that is not under-estimated due to uncertain line-of-sight velocity measurements.*

stars, similar to the SK96 data-set, and the differences are still within the expected uncertainties indicated by the error bar.

The thick solid curve is the dispersion profile of the 3094 stars after merging the four line-of-sight velocity data-sets (§ 2.4.2). Due to uncertainties in the line-of-sight velocity measurements of especially the fainter stars, the latter dispersion profile is (slightly) under-estimated in the outer parts. By sequentially lowering the limit on the line-of-sight velocity errors, we find that below 2.0 km s^{-1} the velocity dispersion (thick dashed curve) converges. Hence, we select the 2163 stars with line-of-sight velocity errors smaller than 2.0 km s^{-1}.

The spatial distribution of these stars is shown in the right panel Fig. 4. In the bottom panels of Fig. 5, the distribution of the line-of-sight velocities (left) and corresponding errors (right) of the $N_{\rm sel} = 2163$ selected stars are shown as filled histograms, on top of the histograms of the $N_{\rm mem} = 3094$ cluster members in the merged data-set.

4   KINEMATICS

We compute the mean velocity fields for the selected stars and correct the kinematic data for perspective rotation and for residual solid-body rotation in the proper motions. At the same time, we place a tight constraint on the inclination. Finally, we calculate the mean velocity dispersion profiles from the corrected kinematic data.
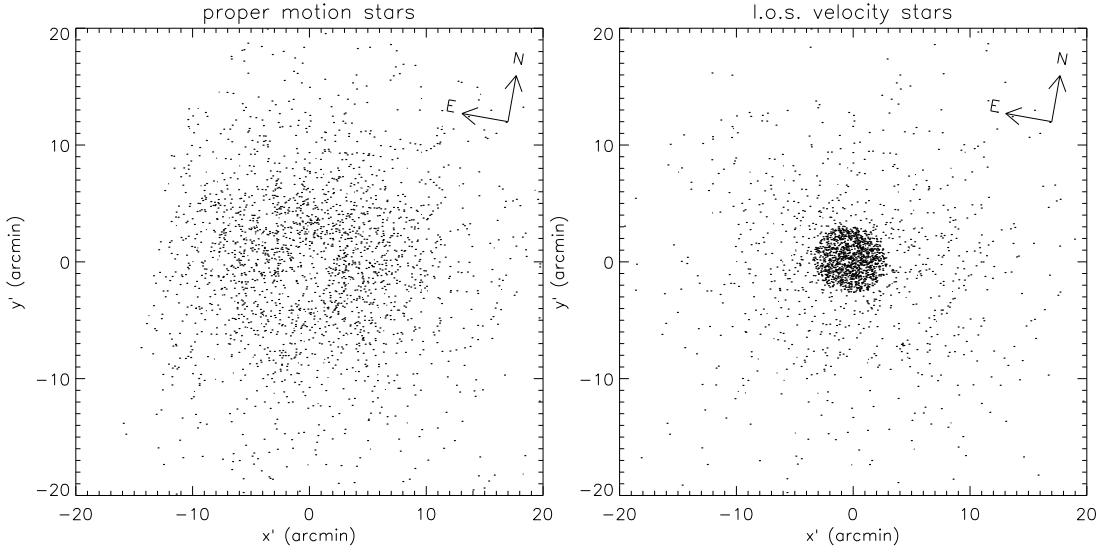
FIGURE 4 — *The stars in ω Cen with proper motion measurements (left) and line-of-sight velocity measurements (right), that are used in our analysis. The stellar positions are plotted as a function of the projected Cartesian coordinates x' and y', with the x'-axis aligned with the observed major axis and the y'-axis aligned with the observed minor axis of ω Cen. The excess of stars with line-of-sight velocities inside the central 3 arcmin in the bottom panel is due to the XGEA data-set.*

4.1 SMOOTHED MEAN VELOCITY FIELDS

The left-most panels of Fig. 6 show the smoothed mean velocity fields for the 2295 selected stars with proper motion measurements and the 2163 selected stars with line-of-sight velocity measurements. This adaptive kernel smoothening is done by selecting for each star its 200 nearest neighbors on the plane of the sky, and then calculating the mean velocity (and higher order velocity moments) from the individual velocity measurements (Appendix A). The contribution of each neighbor is weighted with its distance to the star, using a Gaussian distribution with zero mean and the mean distance of the 200 nearest neighbors as the dispersion.

The top-left panel shows the mean proper motion (in $\mathrm{mas\,yr^{-1}}$) in the major axis x'-direction, i.e., the horizontal component of the streaming motion on the plane of the sky. The grey scale is such that white (black) means that the stars are moving on average to the right (left) and the dashed curve shows the region where the horizontal component of the mean proper motion vanishes. Similarly, the middle-left panel shows the mean proper motion in the minor axis y'-direction, i.e. the vertical component of the streaming motion on the plane of the sky, with white (black) indicating average proper motion upwards (downwards). Finally, the lower-left panel shows the mean velocity (in $\mathrm{km\,s^{-1}}$) along the line-of-sight z'-axis, where white (black) means that the stars are on average receding (approaching). The (dashed) zero-velocity curve is the rotation axis of ω Cen.

Apart from a twist in the (dashed) zero-velocity curve, the latter line-of-sight velocity field is as expected for a (nearly) axisymmetric stellar system. However, both proper motion fields show a complex structure, with an apparently dynamically de-
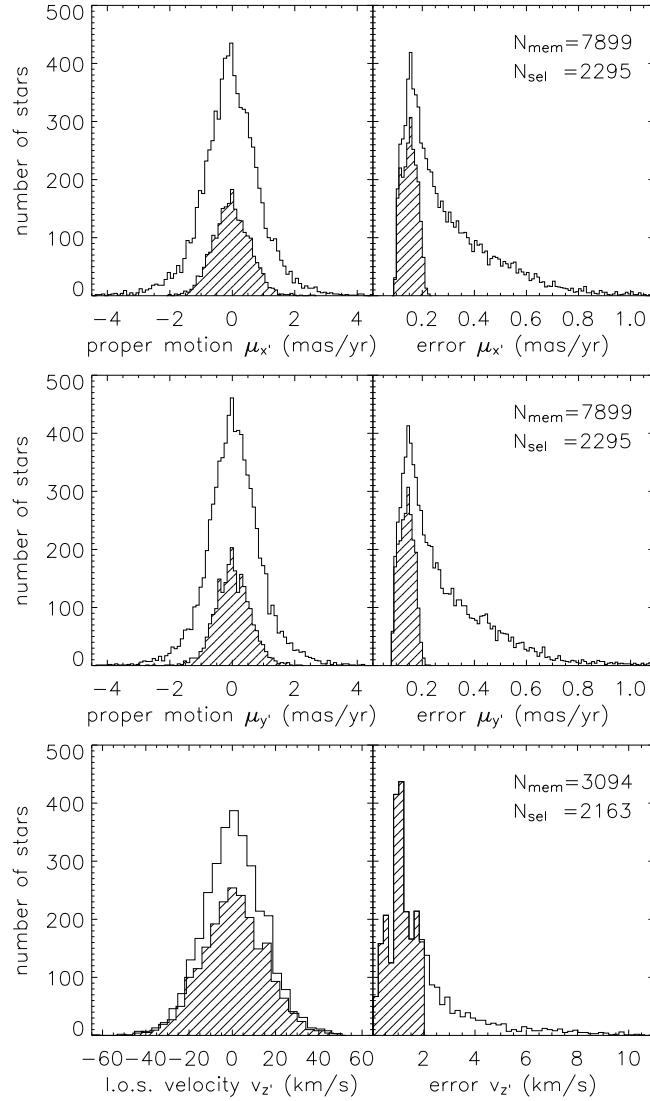
FIGURE 5 — *Histograms of measured velocities (left panels) and corresponding velocity errors (right panels). The proper motion components $\mu_{x'}$ (top panels) and $\mu_{y'}$ (middle panels), in the direction of the observed major and minor axis of ω Cen respectively, come from the photographic plate observations in Paper I. The line-of-sight velocities (lower panels) are taken from four different data-sets ($\S$ 2.2). The shaded histograms for the N_{sel} selected stars ($\S$ 3) are overlayed on the histograms of the N_{mem} cluster member stars.*

coupled inner part, far from axisymmetric. We now show that it is, in fact, possible to bring these different observations into concordance.

4.2   PERSPECTIVE ROTATION

The non-axisymmetric features in the observed smoothed mean velocity fields in the left-most panels of Fig. 6, might be (partly) caused by perspective rotation. Because
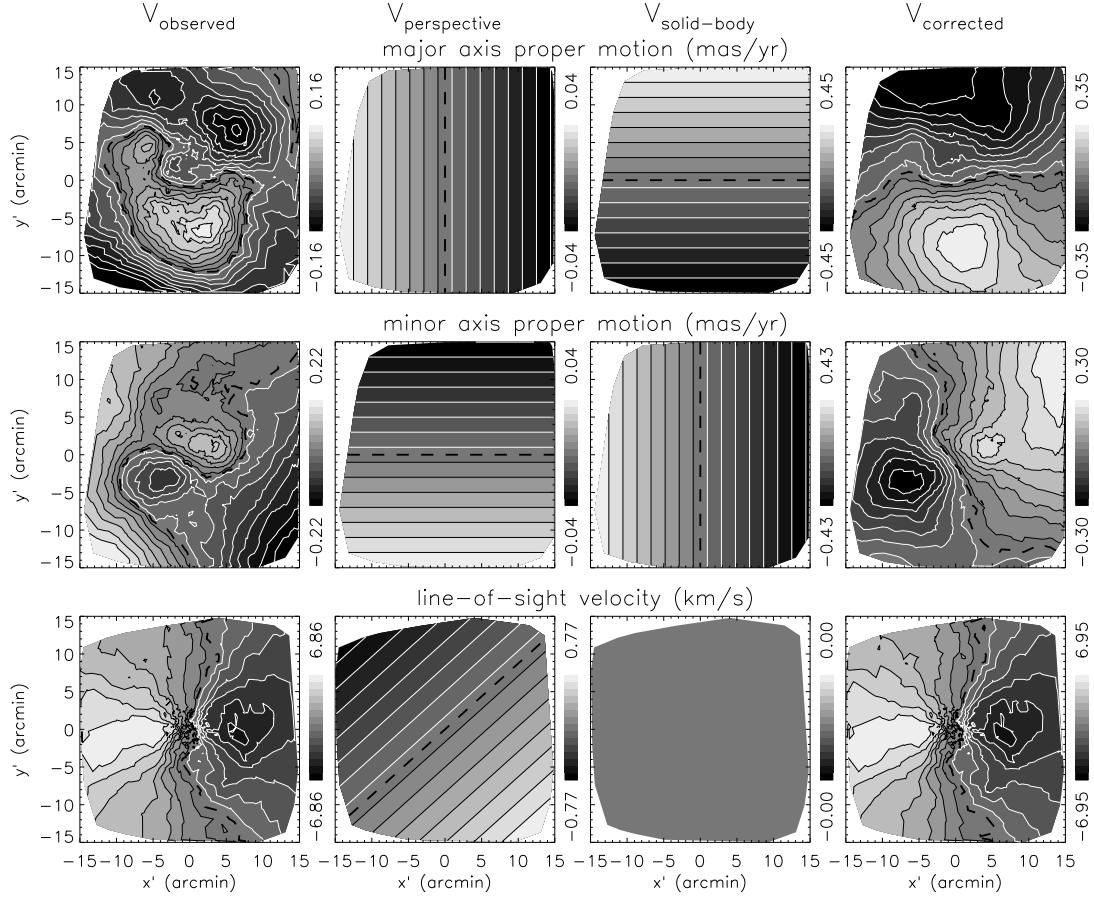
FIGURE 6 — *The mean velocity fields of ω Cen corrected for perspective and solid-body rotation. The individual measurements are smoothed using adaptive kernel smoothening. From top to bottom: The mean ground-based proper motion in the major axis x'-direction and in the minor axis y'-direction, and the mean line-of-sight velocity. From left to right: Observed velocity fields of ω Cen, contribution from perspective rotation, contribution from solid-body rotation and the velocity fields after correcting for both. The perspective rotation is caused by the space motion of ω Cen. The solid-body rotation in the proper motions is due to relative rotation of the first and second epoch photographic plates by an amount of 0.029 mas yr^{-1} arcmin^{-1}. (See p. 249 for a color version of this figure.)*

ω Cen has a large extent on the plane of the sky (with a diameter about twice that of the full moon), its substantial systemic (or space) motion (eq. 2.3) produces a non-negligible amount of apparent rotation: the projection of the space motion onto the principal axis (x', y', z') is different at different positions on the plane of the sky (Feast, Thackeray & Wesselink 1961). We expand this perspective rotation in terms of the reciprocal of the distance D. Ignoring the negligible terms of order $1/D^2$ or smaller, we find the following additional velocities

$$
\begin{array}{rcll}
\mu_{x'}^{\mathrm{pr}} & = & -6.1363 \times 10^{-5}\, x' v_{z'}^{\mathrm{sys}}/D & \mathrm{mas\,yr^{-1}}, \\
\mu_{y'}^{\mathrm{pr}} & = & -6.1363 \times 10^{-5}\, y' v_{z'}^{\mathrm{sys}}/D & \mathrm{mas\,yr^{-1}}, \\
v_{z'}^{\mathrm{pr}} & = & 1.3790 \times 10^{-3} \left(x' \mu_{x'}^{\mathrm{sys}} + y' \mu_{y'}^{\mathrm{sys}} \right) D & \mathrm{km\,s^{-1}},
\end{array}
\qquad (4.1)
$$

with x' and y' in units of arcmin and D in kpc. For the canonical distance of 5 kpc, the systemic motion for ω Cen as given in eq. (2.3) and the data typically extending to 20 arcmin from the cluster center, we find that the maximum amplitude of the perspective rotation for the proper motions is about 0.06 mas yr^{-1} and for the line-of-sight velocity about 0.8 km s^{-1}. These values are a significant fraction of the observed mean velocities (left panels of Fig. 6) and of the same order as the uncertainties in the extracted kinematics (see Appendix B). Therefore, the perspective rotation as shown in the second column panels of Fig. 6, cannot be ignored and we correct the observed stellar velocities by subtracting it. Since we use the more recent and improved values for the systemic proper motion from Paper I, our correction for perspective rotation is different from that of Merritt et al. (1997). The amplitude of the correction is, however, too small to explain all of the complex structure in the proper motion fields and we have to look for an additional cause of non-axisymmetry.

4.3 RESIDUAL SOLID-BODY ROTATION

Van Leeuwen & Le Poole (2002) already showed that a possible residual solid-body rotation component in the ground-based proper motions of Paper I can have an important effect on the kinematics. The astrometric reduction process to measure proper motions removes the ability to observe an overall rotation on the plane of the sky (e.g., Vasilevskis et al. 1979). This solid-body rotation results in a transverse proper motion $v_t = \Omega\,R'$, with Ω the amount of solid-body rotation (in units of mas yr^{-1} arcmin^{-1}) and R' the distance from the cluster center in the plane of the sky (in units of arcmin). Decomposition of v_t along the observed major and minor axis yields

$$
\begin{aligned}
\mu_{x'}^{\mathrm{sbr}} &= +\Omega\,y' \quad \mathrm{mas\,yr}^{-1}, \\
\mu_{y'}^{\mathrm{sbr}} &= -\Omega\,x' \quad \mathrm{mas\,yr}^{-1}.
\end{aligned}
\tag{4.2}
$$

Any other reference point than the cluster center results in a constant offset in the proper motions, and is removed by setting the systemic proper motions to zero. Also an overall expansion (or contraction) cannot be determined from the measured proper motions, and results in a radial proper motion in the plane of the sky. Although both the amount of overall rotation and expansion are in principle free parameters, they can be constrained from the link between the measured (differential) proper motions to an absolute proper motion system, such as defined by the Hipparcos and Tycho-2 catalogues (Perryman et al. 1997; Høg et al. 2000). In Paper I, using the 56 stars in common with these two catalogues, the allowed amount of residual solid-body rotation was determined to be no more than $\Omega = 0.02 \pm 0.02$ mas yr^{-1} arcmin^{-1} and no significant expansion was found.

As the amplitude of the allowed residual solid-body rotation is of the order of the uncertainties in the mean proper motions already close to the center, and can increase beyond the maximum amplitude of the mean proper motions in the outer parts, correcting for it has a very important effect on the proper motions. We use a general relation for axisymmetric objects to constrain Ω, and at the same find a constraint on the inclination.

4.4 THE RESIDUAL SOLID-BODY ROTATION DIRECTLY FROM THE MEAN VELOCITIES

For any axisymmetric system, there is, at each position (x', y') on the plane of the sky, a simple relation between the mean proper motion in the y'-direction $\langle\mu_{y'}\rangle$ and the
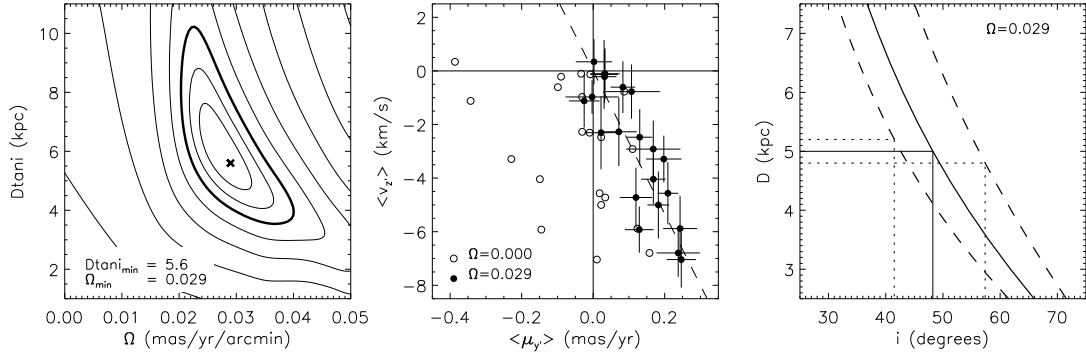
FIGURE 7 — *Constraints on the amount of residual solid-body body rotation Ω and via $D \tan i$, on the distance D (in kpc) and inclination i (in degrees), using the general relation (4.3) for axisymmetric objects. The left panel shows the contour map of the goodness-of-fit parameter $\Delta\chi^2$. The inner three contours are drawn at the 68.3%, 95.4% and 99.7% (thick contour) levels of a $\Delta\chi^2$-distribution with two degrees of freedom. Subsequent contours correspond to a factor of two increase in $\Delta\chi^2$. The overall minimum is indicated by the cross. The middle panel shows the mean line-of-sight velocity $\langle v_{z'} \rangle$ and mean short-axis proper motion $\langle \mu_{y'} \rangle$ within the same polar apertures, before (open circles) and after (filled circles) correction for residual solid-body rotation with the best-fit value of $\Omega = 0.029 \pm 0.004$ mas yr^{-1} arcmin^{-1}. The best-fit value for $D \tan i = 5.6 \, (+1.9/-1.0)$ kpc gives rise to the relation in the right panel (sold line), bracketed (at the 68.3%-level) by the dashed lines. Given the canonical distance of $D = 5.0 \pm 0.2$ kpc, the dotted lines indicate the constraint on inclination of $i = 48 \, (+9/-7)$ degrees.*

mean line-of-sight velocity $\langle v_{z'} \rangle$ (see e.g. Appendix A of Evans & de Zeeuw 1994, hereafter EZ94). Using relation (2.5), with for an axisymmetric system $\langle v_R \rangle = \langle v_z \rangle = 0$, we see that, while the mean velocity component in the x'-direction includes the spatial term $\cos\phi$, those in the y'-direction and line-of-sight z'-direction both contain $\sin\phi$. The latter implies that, by integrating along the line-of-sight to obtain the observed mean velocities, the expressions for $\langle v_{y'} \rangle$ and $\langle v_{z'} \rangle$ only differ by the $\cos i$ and $\sin i$ terms. Going from $\langle v_{y'} \rangle$ to $\langle \mu_{y'} \rangle$ via eq. (2.4), we thus find the following general relation for axisymmetric objects

$$\langle v_{z'} \rangle (x', y') = 4.74 \, D \tan i \, \langle \mu_{y'} \rangle (x', y'), \qquad (4.3)$$

with distance D (in kpc) and inclination i.

This relation implies that, at each position on the plane of the sky, the only difference between the mean short-axis proper motion field and the mean line-of-sight velocity field should be a constant scaling factor equal to $4.74 \, D \tan i$. Comparing the left-most middle and bottom panel in Fig. 6 (V_{observed}), this is far from what we see, except perhaps for the inner part. We ascribe this discrepancy to the residual solid-body rotation, which causes a perturbation of $\langle \mu_{y'} \rangle$ increasing with x' as given in eq. (4.2). In this way, we can objectively quantify the amount of solid body rotation Ω needed to satisfy the above relation (4.3), and at the same time find the best-fit value for $D \tan i$.

To compute uncorrelated values (and corresponding errors) for the mean short-axis proper motion $\langle \mu_{y'} \rangle$ and mean line-of-sight velocity $\langle v_{z'} \rangle$ at the same positions on the plane of the sky, we bin the stars with proper motion and line-of-sight velocity measurements in the same polar grid of apertures (see also Appendix B). We plot the resulting values for $\langle v_{z'} \rangle$ against $\langle \mu_{y'} \rangle$ and fit a line (through the origin) by minimizing

the χ^2, weighted with the errors in both directions (§ 15.3 of Press et al. 1992).

By varying the amount of solid-body rotation Ω and the slope of the line, which is proportional to $D \tan i$ (eq. 4.3), we obtain the $\Delta\chi^2 = \chi^2 - \chi^2_{\min}$ contours in the left panel of Fig. 7. The inner three contours are drawn at the levels containing 68.3%, 95.4% and 99.7% (thick contour) of a $\Delta\chi^2$-distribution with two degrees of freedom[6]. Subsequent contours correspond to a factor of two increase in $\Delta\chi^2$. The overall minimum $\chi^2_{\min}$, indicated by a cross, implies (at the 68.3%-level) a best-fit value of $\Omega = 0.029 \pm 0.004$ mas yr^{-1} arcmin^{-1}. This is fully consistent with the upper limit of $\Omega = 0.02 \pm 0.02$ mas yr^{-1} arcmin^{-1} from Paper I.

The middle panel of Fig. 7 shows that without any correction for residual solid-body rotation, the values for $\langle v_{z'} \rangle$ and $\langle \mu_{y'} \rangle$ are scattered (open circles), while they are nicely correlated after correction with $\Omega = 0.029$ mas yr^{-1} arcmin^{-1} (filled circles). The resulting solid-body rotation, shown in the third column of Fig. 6, removes the cylindrical rotation that is visible in the outer parts of the observed proper motion fields (first column). After subtracting this residual solid-body rotation, together with the perspective rotation (second column), the complex structures disappear, resulting in (nearly) axisymmetric mean velocity fields in the last column. Although the remaining non-axisymmetric features, such as the twist of the (dashed) zero-velocity curve, might indicate deviations from true axisymmetry, they can also be (partly) artifacts of the smoothening, which, especially in the less dense outer parts, is sensitive to the distribution of stars on the plane of the sky.

This shows that the application of eq. (4.3) to the combination of proper motion and line-of-sight measurements provides a powerful new tool to determine the amount of solid body rotation. At the same time, it also provides a constraint on the inclination.

4.5   CONSTRAINT ON THE INCLINATION

From the left panel of Fig. 7 we obtain (at the 68.3%-level) a best-fit value for $D \tan i$ of $5.6\,(+1.9/-1.0)$ kpc. The right panel shows the resulting relation (solid line) between the distance D and the inclination i, where the dashed lines bracket the 68.3%-level uncertainty. If we assume the canonical value $D = 5.0 \pm 0.2$ kpc, then the inclination is constrained to $i = 48\,(+9/-7)$ degrees.

Although we apply the same polar grid to the proper motions and line-of-sight velocities, the apertures contain different (numbers of) stars. To test that this does not significantly influence the computed average kinematics and hence the above results, we repeated the analysis but now only include the 718 stars for which both the proper motions and line-of-sight velocity are measured. The results are equivalent, but less tightly constrained due to the smaller number of apertures.

Van Leeuwen & Le Poole (2002) compared, for different values for the amount of residual solid-body rotation Ω, the shape of the radial profile of the mean transverse component of proper motions from Paper I, with that of the mean line-of-sight velocities calculated by Merritt et al. (1997) from the line-of-sight velocity data-set of M97. They found that $\Omega \sim 0.032$ mas yr^{-1} arcmin^{-1} provides a plausible agreement. Next, assuming a distribution for the density and the rotational velocities in the cluster, they computed projected transverse proper motion and line-of-sight velocity profiles,

---

[6]For a Gaussian distribution with dispersion σ, these percentages correspond to the 1σ, 2σ and 3σ confidence intervals respectively. For the (asymmetric) χ^2-distribution there is in general no simple relation between dispersion and confidence intervals. Nevertheless, the 68.3%, 95.4% and 99.7% levels of the χ^2-distribution are often referred to as the 1σ, 2σ and 3σ levels.

and by comparing them to the observed profiles, they derived a range for the inclination i from 40 to 60 degrees. Their results are consistent with our best-fit values $\Omega = 0.029 \pm 0.004$ mas yr^{-1} arcmin^{-1} and $i = 48\,(+9/-7)$ degrees. Our method is based on a general relation for axisymmetric objects, without any further assumptions about the underlying density and velocity distribution. Moreover, instead of comparing shapes of mean velocity profiles, we actually fit the mean velocity fields.

In the above analysis, we assume that all of the solid-body rotation in the proper motion is the result of a (non-physical) residual from the photographic plate reduction in Paper I. This raises the question what happens if a (physical) solid-body rotation component is present in ω Cen. Such a solid-body rotation component is expected to be aligned with the intrinsic rotation axis, inclined at about 48°, and therefore also present in the line-of-sight velocities. Except for the perspective rotation correction, we leave the mean line-of-sight velocities in the above analysis unchanged, so that any such solid-body rotation component should also remain in the proper motion.

Still, since we are fitting the residual solid-body rotation Ω and the slope $D \tan i$ simultaneously, they can become (partly) degenerate. Combining eq. (4.2) with (4.5), we obtain the best-fit values for $D \tan i$ and Ω by minimizing

$$\chi^2 = \sum_j^n \frac{\left[\langle v_{z'}^{\mathrm{obs}} \rangle_j - 4.74\, D \tan i \, \left(\langle \mu_{y'}^{\mathrm{obs}} \rangle_j + \Omega\, x'_j \right) \right]^2}{\left[\Delta \langle v_{z'}^{\mathrm{obs}} \rangle_j \right]^2 + \left[4.74\, D \tan i \, \Delta \langle \mu_{y'}^{\mathrm{obs}} \rangle_j \right]^2}, \qquad (4.4)$$

where $\langle v_{z'}^{\mathrm{obs}} \rangle_j$ and $\langle \mu_{y'}^{\mathrm{obs}} \rangle_j$ are respectively the observed mean line-of-sight velocity and the observed mean proper motion in the y'-direction, measured in aperture j of a total of n apertures, with their centers at x'_j. $\Delta \langle v_{z'}^{\mathrm{obs}} \rangle_j$ and $\Delta \langle \mu_{y'}^{\mathrm{obs}} \rangle_j$ are the corresponding measurement errors. Suppose now the extreme case that all of the observed mean motion is due to solid-body rotation: an amount of Ω_0 residual solid-body rotation in the plane of the sky, and an amount of ω_0 intrinsic solid-body rotation, around the intrinsic z-axis in ω Cen, which we assume to be inclined at i_0 degrees. At a distance D_0, the combination yields per aperture $\langle v_{z'}^{\mathrm{obs}} \rangle_j = 4.74 D_0 \omega_0 \sin i_0 x'_j$ and $\langle \mu_{y'}^{\mathrm{obs}} \rangle_j = (\omega_0 \cos i_0 - \Omega_0) x'_j$. Substitution of these quantities in the above eq. (4.4), and ignoring the (small) variations in the measurements errors, yields that $\chi^2 = 0$ if

$$D \tan i = D_0 \tan i_0 \left[1 + \frac{\Omega - \Omega_0}{\omega_0 \cos i_0} \right]^{-1}. \qquad (4.5)$$

This implies a degeneracy between $D \tan i$ and Ω, which in the left panel of Fig. 7, would result in the same minimum all along a curve. However, in the case the motion in ω Cen consists of more than only solid-body rotation, this degeneracy breaks down and we expect to find a unique minimum. The latter seems to be the case here, and we conclude that the degeneracy and hence the intrinsic solid-body rotation are not dominant, if present at all.

4.6 MEAN VELOCITY DISPERSION PROFILES

In Fig. 8, we show the mean velocity dispersion profiles of the radial $\sigma_{R'}$ (dotted) and tangential $\sigma_{\theta'}$ (dashed) components of the proper motions, together with the line-of-sight velocity dispersion $\sigma_{z'}$ (solid). The dispersions are calculated along concentric rings from the selected sample of 2295 stars with proper motions corrected for perspective and residual solid-body rotation and 2163 stars with line-of-sight velocities
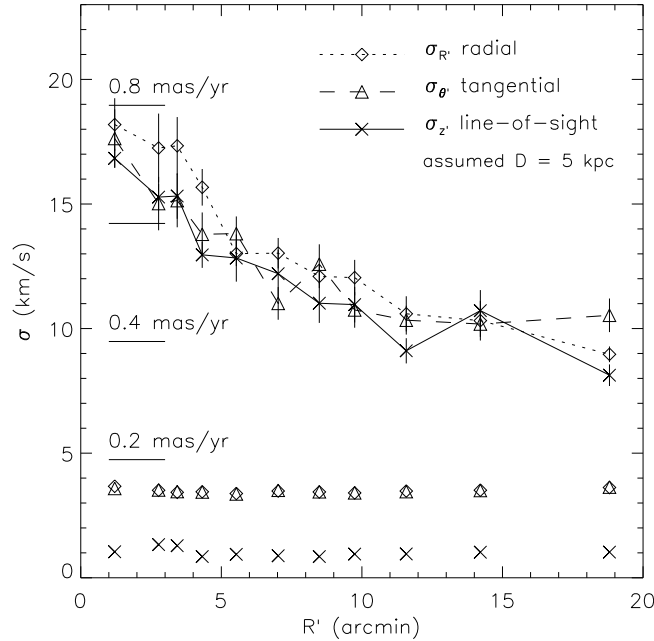
FIGURE 8 — *Mean velocity dispersion profiles calculated along concentric rings. Assuming the canonical distance of 5 kpc, the profiles of the radial $\sigma_{R'}$ (dotted curve with diamonds) and tangential $\sigma_{\theta'}$ (dashed curve with triangles) components of the proper motion dispersion are converted into the same units of $km\,s^{-1}$ as the profile of the line-of-sight velocity dispersion $\sigma_{z'}$ (solid curve with crosses). The horizontal lines indicate the corresponding scale in $mas\,yr^{-1}$. The mean velocity error per ring is indicated below the profiles by the corresponding symbols. The diamonds and triangles mostly overlap, as the errors of the radial and tangential components are nearly similar.*

corrected for perspective rotation. We obtain similar mean velocity dispersion profiles if we only use the 718 stars for which both proper motions and line-of-sight velocity are measured. We assume the canonical distance of 5 kpc to convert the proper motion dispersion into units of $km\,s^{-1}$, while the black horizontal lines indicate the corresponding scale in units of $mas\,yr^{-1}$. Below the profiles, the symbols represent the corresponding mean velocity error per ring, showing that the accuracy of the line-of-sight velocity measurements (crosses) is about four times better than the proper motion measurements (diamond and triangles, which mostly overlap since the errors for the two components are similar).

In § 3.1, we already noticed that since the (smoothed) profile of the major-axis proper motion dispersion $\sigma_{x'}$ lies on average above that of the minor-axis proper motion dispersion $\sigma_{y'}$ (Fig. 1 and 2), the velocity distribution of ω Cen cannot be fully isotropic. By comparing in Fig. 8 the radial (dotted) with the tangential (dashed) component of the proper motion dispersion, ω Cen seems to be radial anisotropic towards the center, and there is an indication of tangential anisotropy in the outer parts. Moreover, if ω Cen would be isotropic, the line-of-sight velocity dispersion profile (blue) would have to fall on top of the proper motion dispersion profiles if scaled with the correct distance. A scaling with a distance lower than the canonical 5 kpc

is needed for the line-of-sight dispersion profile to be on average the same as those of both proper motion components.

Hence, it is not surprising that we find a distance as low as $D = 4.6 \pm 0.2$ kpc from the ratio of the average line-of-sight velocity dispersion and the average proper motion dispersion (Appendix C). This often used simple distance estimate is only valid for spherical symmetric objects. Whereas the averaged observed flattening for ω Cen is already as low as $q' = 0.879 \pm 0.007$ (Geyer et al. 1983), an inclination of around $48°$ (§ 4.5), implies an intrinsic axisymmetric flattening $q < 0.8$.

A model with a constant oblate velocity ellipsoid as in Appendix C, allows for offsets between the mean velocity dispersion profiles. However, the model is not suitable to explain the observed variation in anisotropy with radius. Therefore, we use in what follows Schwarzschild's method to build general axisymmetric anisotropic models.

5   SCHWARZSCHILD'S METHOD

We construct axisymmetric dynamical models using Schwarzschild's (1979) orbit superposition method. This approach is flexible and efficient and does not require any assumptions about the degree of velocity anisotropy. The only crucial approximations are that the object is collisionless and stationary. While these assumptions are generally valid for a galaxy, they may not apply to a globular cluster. The central relaxation time of ω Cen is a few times 10^9 years and the half-mass relaxation time a few times 10^{10} years (see also Fig. 21 below). The collisionless approximation should therefore be fairly accurate.

The implementation that we use here is an extension of the method presented in Verolme et al. (2002). In the next subsections, we outline the method and describe the extensions.

5.1   MASS MODEL

Schwarzschild's method requires a mass parameterization, which we obtain by using the Multi-Gaussian Expansion method (MGE; Monnet, Bacon & Emsellem 1992; Emsellem, Monnet & Bacon 1994; Cappellari 2002). The MGE-method tries to find the collection of two-dimensional Gaussians that best reproduces a given surface brightness profile or a (set) of images. Typically, of the order of ten Gaussians are needed, each with three free parameters: the central surface brightness $\Sigma_{0,j}$, the dispersion along the observed major axis σ'_j and the observed flattening q'_j. Even though Gaussians do not form a complete set of functions, in general the surface brightness is well fitted (see also Fig. 12). Moreover, the MGE-parameterization has the advantage that the deprojection can be performed analytically once the viewing angles (in this case the inclination) are given. Also many intrinsic quantities such as the potential and accelerations can be calculated by means of simple one-dimensional integrals.

5.2   GRAVITATIONAL POTENTIAL

We deproject the set of best-fitting Gaussians by assuming that the cluster is axisymmetric and by choosing a value of the inclination i. The choice of a distance D to the object then allows us to convert angular distances to physical units, and luminosities are transformed to masses by multiplying with the mass-to-light ratio M/L.

The latter quantity is often assumed to be independent of radius. In the inner regions of most galaxies, where two-body relaxation does not play an important role,

this often is a valid assumption. Generally, globular clusters have much shorter relaxation times and may therefore show significant M/L-variations. This has been confirmed for post core-collapse clusters such as M15 (e.g., Dull et al. 1997; van den Bosch et al. 2006). However, ω Cen has a relatively long relaxation time of $> 10^9$ years, implying that little mass segregation has occurred and the mass-to-light ratio should be nearly constant with radius. In our analysis we assume a constant M/L, but we also investigate possible M/L-variations.

The stellar potential is then calculated by applying Poisson's equation to the intrinsic density. The contribution of a dark object such as a collection of stellar remnants or a central black hole may be added at this stage. On the basis of the relation between the black hole mass and the central dispersion (e.g., Tremaine et al. 2002), globular clusters might be expected to harbor central black holes with intermediate mass of the order 10^3–10^4 M$_\odot$ (e.g., van der Marel 2004). With a central dispersion of nearly 20 km s^{-1}, the expected black hole mass for ω Cen would be $\sim 10^4$ M$_\odot$. The spatial resolution that is required to observe the kinematical signature of such a black hole is of the order of its radius of influence, which is around 5 arcsec (at the canonical distance of 5 kpc). This is approximately an order of magnitude smaller than the resolution of the ground-based observations we use in our analysis, so that our measurements are insensitive to such a small mass. Hence, we do not include a black hole in our dynamical models of ω Cen.

5.3   INITIAL CONDITIONS AND ORBIT INTEGRATION

After deriving the potential and accelerations, the next step is to find the initial conditions for a representative orbit library. This orbit library must include all types of orbits that the potential can support, to avoid any bias. This is done by choosing orbits through their integrals of motion, which, in this case, are the orbital energy E, the vertical component of the angular momentum L_z and the effective third integral I_3.

For each energy E, there is one circular orbit in the equatorial plane, with radius R_c that follows from $E = \Phi + \frac{1}{2} R_c \partial \Phi / \partial R_c$ for $z = 0$, and with $\Phi(R, z)$ the underlying (axisymmetric) potential. We sample the energy by choosing the corresponding circular radius R_c from a logarithmic grid. The minimum radius of this grid is determined by the resolution of the data, while the maximum radius is set by the constraint that ≥ 99.9 per cent of the model mass should be included in the grid. L_z is sampled from a linear grid in $\eta = L_z / L_{\mathrm{max}}$, with L_{max} the angular momentum of the circular orbit. I_3 is parameterized by the starting angle of the orbit and is sampled linearly between zero and the initial position of the so-called thin tube orbit (see Fig. 3 of Cretton et al. 1999).

The orbits in the library are integrated numerically for 200 times the period of a circular orbit with energy E. In order to allow for comparison with the data, the intrinsic density, surface brightness and the three components of the projected velocity are stored on grids. During grid storage, we exploit the symmetries of the projected velocities by folding around the projected axes and store the observables only in the positive quadrant ($x' \geq 0, y' \geq 0$). Since the sizes of the polar apertures on which the average kinematic data is computed (Fig. 13) are much larger than the typical seeing FWHM (1–2 arcsec), we do not have to store the orbital properties on an intermediate grid and after orbit integration convolve with the point spread function (PSF). Instead, the orbital observables are stored directly onto the polar apertures.

5.4 FITTING TO THE OBSERVATIONS

After orbit integration, the orbital predictions are matched to the observational data. We determine the superposition of orbits whose properties best reproduce the observations. If O_{ij} is the contribution of the jth orbit to the ith constraint point, this problem reduces to solving for the orbital weights γ_j in

$$\sum_j^{N_O} \gamma_j O_{ij} = C_i, \qquad i = 1, \ldots, N_C, \tag{5.1}$$

where N_O is the number of orbits in the library, N_C is the number of constraints to be reproduced and C_i is the ith constraint. Since γ_j determines the mass of each individual orbit in this superposition, it is subject to the additional condition $\gamma_j \geq 0$.

Eq. (5.1) can be solved by using linear or quadratic programming (e.g., Schwarzschild 1979, 1982, 1993; Vandervoort 1984; Dejonghe 1989), maximum entropy methods (e.g., Richstone & Tremaine 1988; Gebhardt et al. 2003) or with a linear least-squares solver [e.g., Non-Negative Least-Squares (NNLS), Lawson & Hanson 1974], which was used in many of the spherical and axisymmetric implementations (e.g., Rix et al. 1997; van der Marel et al. 1998; Cretton et al. 1999; Cappellari et al. 2002; Verolme et al. 2002; Krajnović et al. 2005), and is also used here. NNLS has the advantage that it is guaranteed to find the global best-fitting model and that it converges relatively quickly.

Due to measurement errors, incorrect choices of the model parameters and numerical errors, the agreement between model and data is never perfect. We therefore express the quality of the solution in terms of χ^2, which is defined as

$$\chi^2 = \sum_{i=1}^{N_c} \left(\frac{C_i^\star - C_i}{\Delta C_i} \right)^2 . \tag{5.2}$$

Here, $C_i^\star$ is the model prediction of the constraint C_i and ΔC_i is the associated error. The value of χ^2 for a single model is of limited value, since the true number of degrees of freedom is generally not known. On the other hand, the difference in χ^2 between a model and the overall minimum value, $\Delta\chi^2 = \chi^2 - \chi^2_{\min}$, is statistically meaningful (see Press et al. 1992, § 15.6), and we can assign the usual confidence levels to the $\Delta\chi^2$ distribution. The probability that a given set of model parameters occurs can be measured by calculating $\Delta\chi^2$ for models with different values of these model parameters. We determine the overall best-fitting model by searching through parameter space.

The orbit distribution for the best-fitting model may vary rapidly for adjacent orbits, which corresponds to a distribution function that is probably not realistic. This can be prevented by imposing additional regularization constraints on the orbital weight distribution. This is usually done by minimizing the nth-order partial derivatives of the orbital weights $\gamma_j(E, L_z, I_3)$, with respect to the integrals of motion E, L_z and I_3. The degree of smoothing is determined by the order n and by the maximum value Δ that the derivatives are allowed to have, usually referred to as the regularization error. Since the distribution function is well recovered by minimizing the second order derivatives ($n = 2$) and smoothening with $\Delta = 4$ (e.g., Verolme & de Zeeuw 2002; Krajnović et al. 2005; Chapter 4), we adopt these values.

6 TESTS

Before applying our method to observational data, we test it on a theoretical model, the axisymmetric power-law model (EZ94).

6.1 THE POWER-LAW MODEL

The potential Φ of the power-law model is given by

$$\Phi(R, z) = \frac{\Phi_0 \, R_c^\beta}{\left(R_c^2 + R^2 + z^2 q_\Phi^{-2}\right)^{\beta/2}},$$
(6.1)

in which (R, z) are cylindrical coordinates, Φ_0 is the central potential, R_c is the core radius and q_Φ is the axial ratio of the spheroidal equipotentials. The parameter β controls the logarithmic gradient of the rotation curve at large radii.

   The mass density that follows from applying Poisson's equation to eq. (6.1) can be expanded as a finite sum of powers of the cylindrical radius R and the potential Φ. Such a power-law density implies that the *even* part of the distribution function is a power-law of the two integrals energy E and angular momentum L_z. For the *odd* part of the distribution function, which defines the rotational properties, a prescription for the stellar streaming is needed. We adopt the prescription given in eq. (2.11) of EZ94, with a free parameter k controlling the strength of the stellar streaming, so that the odd part of the distribution function is also a simple power-law of E and L_z. Due to the simple form of the distribution function, the calculation of the power-law observables is straightforward. Analytical expressions for the surface brightness, the three components of the mean velocity and velocity dispersion are given in eqs (3.1)–(3.8) of EZ94.

6.2 OBSERVABLES

We choose the parameters of the power-law model such that its observable properties resemble those of ω Cen. We use $\Phi_0 = 2500$ km^2 s^{-2}, which sets the unit of velocity of our models, and a core radius of $R_c = 2.5$ arcmin, which sets the unit of length. For the flattening of the potential we take $q_\Phi = 0.95$ and we set $\beta = 0.5$, so that the even part of the distribution function is positive (Fig. 1 of EZ94). The requirement that the total distribution function (even plus odd part) should be non-negative places an upper limit on the (positive) parameter k. This upper limit $k_{\max}$ is given by eq. (2.22) of EZ94[7]. Their eq. (2.24) gives the value k_{iso} for which the power-law model has a nearly isotropic velocity distribution. In our case $k_{\max} = 1.38$ and $k_{\mathrm{iso}} = 1.44$. We choose $k = 1$, i.e., a power-law model that has a (tangential) anisotropic velocity distribution.

   Furthermore, we use an inclination of $i = 50°$, a mass-to-light ratio of $M/L = 2.5$ M$_\odot$/L$_\odot$ and a distance of $D = 5$ kpc. At this inclination the projected flattening of the potential is $q_\Phi' = 0.97$. The isocontours of the projected surface density are more flattened. Using eq. (2.9) of Evans (1994), the central and asymptotic axis ratios of the isophotes are respectively $q_0' = 0.96$ and $q_\infty' = 0.86$, i.e., bracketing the average observed flattening of ω Cen of $q' = 0.88$ (Geyer et al. 1983).

   Given the above power-law parameters, we calculate the three components of the mean velocity V and velocity dispersion σ on a polar grid of 28 apertures, spanning a radial range of 20 arcmin. Because of axisymmetry we only need to calculate the observables in one quadrant on the plane of the sky, after which we reflect the results

---

[7]The definition of χ has a typographical error and should be replaced by $\chi = (1 - \beta/2)/|\beta|$.
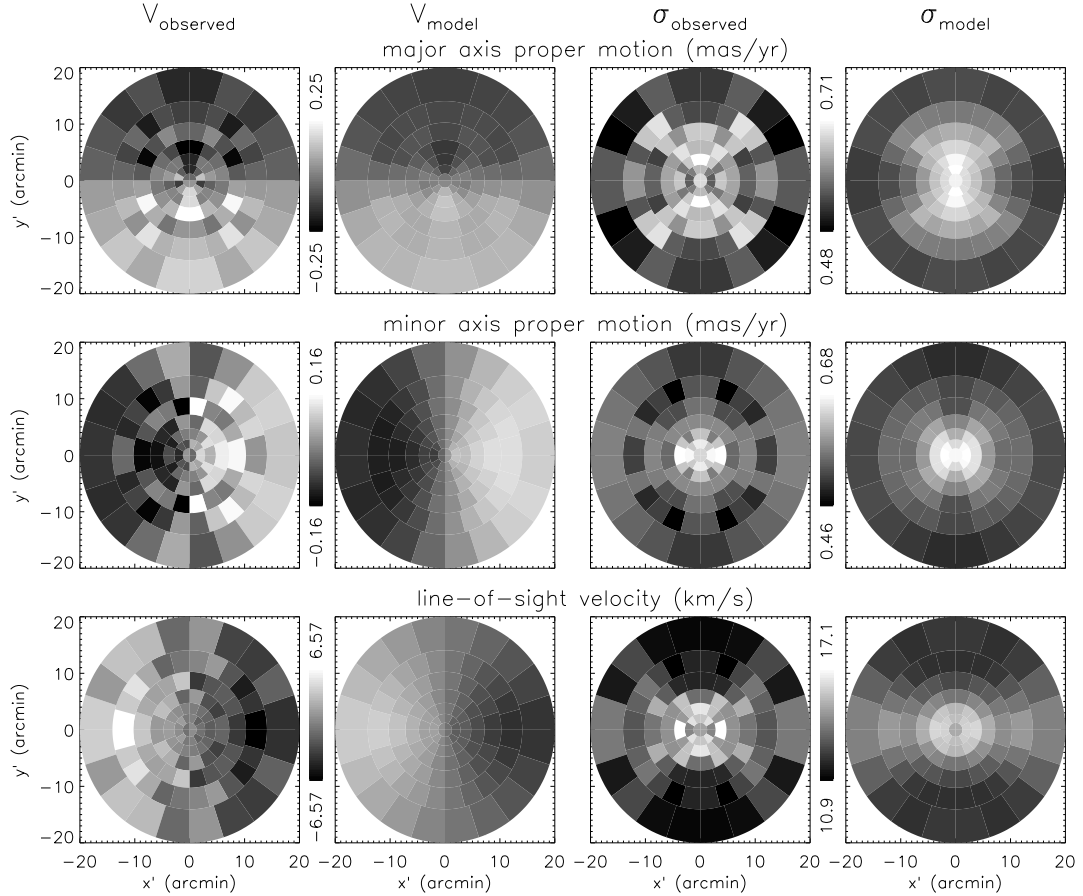
FIGURE 9 — *Mean velocity and velocity dispersion calculated from a power-law model (first and third column) and from the best-fit dynamical Schwarzschild model (second and fourth column). The parameters of the power-law model are chosen such that its observables resemble those of ω Cen, including the level of noise, which is obtained by randomizing the observables according to the uncertainties in the measurements of ω Cen (see § 6.2 and Appendix B for details). The average proper motion kinematics in the x'-direction (top row) and y'-direction (middle row), and the average mean line-of-sight kinematics (bottom row), calculated in polar apertures in the first quadrant, are unfolded to the other three quadrants to facilitate the visualization.*

to the other quadrants. Next, we use the relative precisions $\Delta V/\sigma \sim 0.11$ and $\Delta\sigma/\sigma \sim 0.08$ as calculated for ω Cen (Appendix B), multiplied with the calculated σ for the power-law model, to attach an error to the power-law observables in each aperture. Finally, we perturb the power-law observables by adding random Gaussian deviates with the corresponding errors as standard deviations.

Without the latter randomization, the power-law observables are as smooth as those predicted by the dynamical Schwarzschild models, so that the goodness-of-fit parameter χ^2 in eq. (5.2), approaches zero. Such a perfect agreement never happens for real data. Including the level of noise representative for ω Cen, allows us to use χ^2 to not only investigate the recovery of the power-law parameters, but, at the same

time, also asses the accuracy with which we expect to measure the corresponding parameters for ω Cen itself.

The resulting mean velocity V_{observed} and velocity dispersion σ_{observed} fields for the power-law model are shown in respectively the first and third column of Fig. 9. They are unfolded to the other three quadrants to facilitate the visualization.

6.3   Schwarzschild models

We construct axisymmetric Schwarzschild models based on the power-law potential (6.1). We calculate a library of 2058 orbits by sampling 21 energies E, 14 angular momenta L_z and 7 third integrals I_3. In this way, the number and variety of the library of orbits is large enough to be representative for a broad range of stellar systems, and the set of eqs (5.1) is still solvable on a machine with 512 Mb memory (including regularization constraints).

The resulting three-integral Schwarzschild models include the special case of dependence on only E and L_z like for the power-law models. Schwarzschild's method requires that the orbits in the library are sampled over a range that includes most of the total mass, whereas all power-law models have infinite mass. To solve this problem at least partially, we ensure that there are enough orbits to constrain the observables at all apertures. We distribute the orbits logarithmically over a radial range from 0.01 to 100 arcmin (five times the outermost aperture radius) and fit the intrinsic density out to a radius of 10^5 arcmin. The orbital velocities are binned in histograms with 150 bins, at a velocity resolution of 2 km s^{-1}.

To test whether and with what precision we can recover the input distance of $D = 5$ kpc, the inclination of $i = 50°$ and the mass-to-light ratio $M/L = 2.5 \text{ M}_\odot/\text{L}_\odot$, we calculate models for values of D between 3.5 and 6.5 kpc, i between $35°$ (the asymptotic isophotal axis ratio $q'_\infty = 0.86$ implies that $i > 30°$) and $70°$, and M/L between 1.5 and $3.5 \text{ M}_\odot/\text{L}_\odot$. Additionally, to test how strongly the best-fitting parameters depend on the underlying mass model, we also vary the flattening of the power-law potential q_Φ between 0.90 and 1.00. We then fit each of the dynamical models simultaneously to the calculated observables of the power-law model (with $q_\Phi = 0.95$). Comparing these calculated observables with those predicted by the Schwarzschild models, results for each fitted Schwarzschild model in a goodness-of-fit parameter χ^2. We use this value to find the best-fit Schwarzschild model and to determine the accuracy of the corresponding best-fit parameters.

Calculating the observables for all orbits in the library requires about an hour on a 1 GHz machine with 512 MB memory and the NNLS-fit takes about half an hour. No distinct models need to be calculated for different values of M/L, as a simple velocity scaling prior to the NNLS-fit is sufficient. Making use of (a cluster of) about 30 computers, the calculations for the full four-parameter grid of Schwarzschild models takes a few days.

6.4   Distance, inclination and mass-to-light ratio

The Schwarzschild model that best fits the calculated power-law observables is the one with the (overall) lowest χ^2-value. After subtraction of this minimum value, we obtain $\Delta\chi^2$ as function of the three parameters D, i and M/L (with $q_\Phi = 0.95$ fixed). To visualize this three-dimensional function, we calculate for a pair of parameters, say D and i, the minimum in $\Delta\chi^2$ as function of the remaining parameter, M/L in
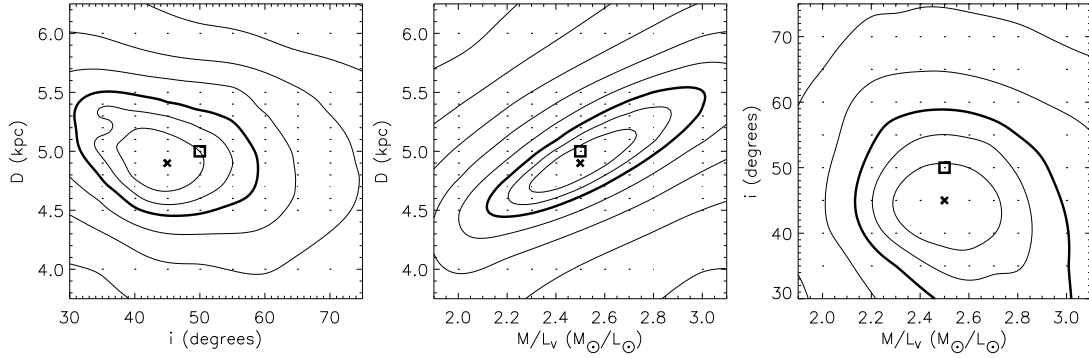
FIGURE 10 — *The (marginalized) goodness-of-fit parameter $\Delta\chi^2$ as a function of distance D, inclination i and mass-to-light ratio M/L_V, for different Schwarzschild model fits (indicated by the dots) to an axisymmetric power-law model with observables resembling those of ω Cen (see text for details). The χ^2-values are offset such that the overall minimum, indicated by the cross, is zero. The contours are drawn at the confidence levels for a $\Delta\chi^2$-distribution with three degrees of freedom, with inner three contours corresponding to the 68.3%, 95.4% and 99.7% (thick contour) confidence levels. Subsequent contours correspond to a factor of two increase in $\Delta\chi^2$. The input parameters $D = 5.0$ kpc, $i = 50°$ and $M/L = 2.5$ $M_\odot/L_\odot$, indicated by the open square, are recovered within the 68.3% confidence levels.*

this case. The contour plot of the resulting marginalized $\Delta\chi^2$ is shown in the left panel of Fig. 10. The dots indicate the values at which Schwarzschild models have been constructed and fitted to the power-law observables. The contours are drawn at the confidence levels for a $\Delta\chi^2$-distribution with three degrees of freedom, with inner three contours corresponding to the 68.3%, 95.4% and 99.7% (thick contour) confidence levels. Subsequent contours correspond to a factor of two increase in $\Delta\chi^2$. The minimum ($\Delta\chi^2 = 0$) is indicated by the cross. Similarly, we show in the middle and left panel the contour plots of $\Delta\chi^2$ marginalized for respectively the pair D and M/L and the pair i and M/L.

The input parameters $D = 5.0$ kpc, $i = 50°$ and $M/L = 2.5$ $M_\odot/L_\odot$, indicated by the open square, are well recovered. The mean velocity V_{model} and velocity dispersion σ_{model} predicted by the best-fit Schwarzschild model are shown in the second and fourth column of Fig. 9. The corresponding power-law observables are well reproduced within the error bars.

Since the parameters of the power-law model are chosen such that its observables and corresponding errors resemble those of ω Cen, the contours in Fig. 10 provide an estimate of the precision with which we expect to measure the best-fitting parameters for ω Cen. At the 68.3%-level (99.7%-level) the distance D, inclination i and mass-to-light ratio M/L are retrieved with an accuracy of respectively 6 (11), 9 (18), 13 (28) per cent. Due the additional complication of infinite mass in the case of the power-law models, these estimates most likely are upper limits to the precision we expect to achieve for ω Cen. This holds especially for the inclination and the mass-to-light ratio as they are sensitive to how well the mass model is fitted. The distance is mainly constrained by the kinematics, so that the corresponding accuracy is probably an accurate estimate of the precision with which we expect to measure the distance to ω Cen.
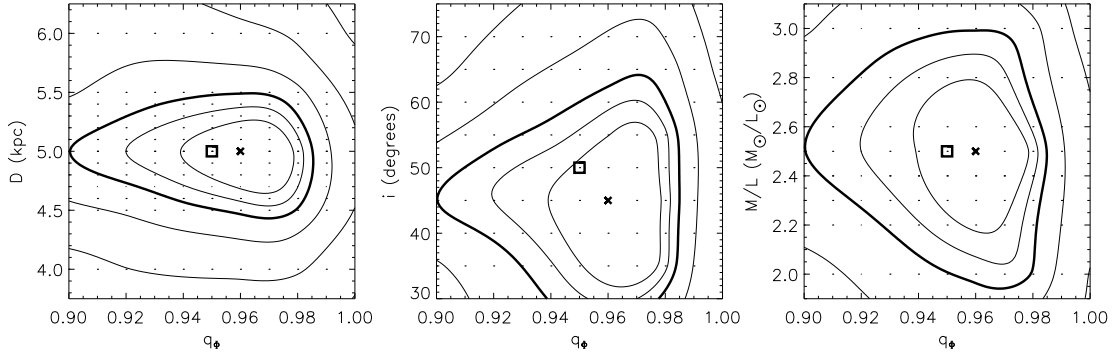
FIGURE 11 — *The (marginalized) goodness-of-fit parameter $\Delta\chi^2$ as a function of distance D, inclination i and mass-to-light ratio M/L against the flattening q_Φ of the underlying potential, for different Schwarzschild model fits (indicated by the dots) to the observables of an axisymmetric power-law model resembling those of ω Cen. The contours are as in Fig. 10, but for a $\Delta\chi^2$-distribution with four degrees of freedom. The cross indicates the overall best-fit model ($\Delta\chi^2 = 0$). The input parameters of the power-law model, $q_\Phi = 0.95$, $D = 5.0$ kpc, $i = 50°$ and $M/L = 2.5$ M$_\odot$/L$_\odot$, are indicated by the open square. The input parameters are recovered within the 68.3% confidence levels, even for mass models that assume a (slightly) incorrect value for the flattening. However, spherical models ($q_\Phi = 1.0$) are strongly ruled out.*

6.5   Flattening

The above investigation of the recovery of the global parameters D, i and M/L is for a known mass model, given by the power-law potential (6.1). In general, we obtain the mass model from a MGE-parameterization of the observed surface brightness (§ 5.1). There is no guarantee that the resulting MGE model provides an accurate description of the true mass distribution. We tested the effect of an incorrect mass model on the best-fit parameters by varying the flattening q_Φ of the power-law potential while keeping the calculated observables (for the power-law model with $q_\Phi = 0.95$) fixed.

Since we use these same values for the other power-law parameters ($\Phi_0 = 2500$ km^2 s^{-2}, $R_c = 2.5$ arcmin, $\beta = 0.5$ and $k = 1$), we have to be careful that by varying q_Φ the model is still physical, i.e., that the underlying distribution function is non-negative. For these parameters and q_Φ between 0.9 and 1.0 this is the case (EZ94).

As before, for all Schwarzschild models we calculate $\Delta\chi^2$, which is now a function of the four parameters D, i, M/L and q_Φ. In the three panels of Fig. 11, we show $\Delta\chi^2$ marginalized for respectively D, i and M/L against q_Φ. The symbols and contours are as in Fig. 10, but now for a $\Delta\chi^2$-distribution with four degrees of freedom. The input parameters of the power-law model (indicated by an open square) are $q_\Phi = 0.95$, $D = 5.0$ kpc, $i = 50°$ and $M/L = 2.5$ M$_\odot$/L$_\odot$.

The distance D is well constrained around the input value, even at q_Φ value that are different from the true value of 0.95. This implies that the best-fitting distance is accurate even for mass models that assume a (slightly) incorrect value for the flattening. Whereas a potential with a flattening as low as 0.90 still (just) falls within the contour at the 99.7%-level, we conclude, as in § 4.6, that spherical models ($q_\Phi = 1$) are strongly ruled out. The middle and right panel of Fig. 11 show that the results for respectively the mass-to-light M/L and inclination i are similar, although, as before, they are less well constrained due to the infinite mass of the power-law models.
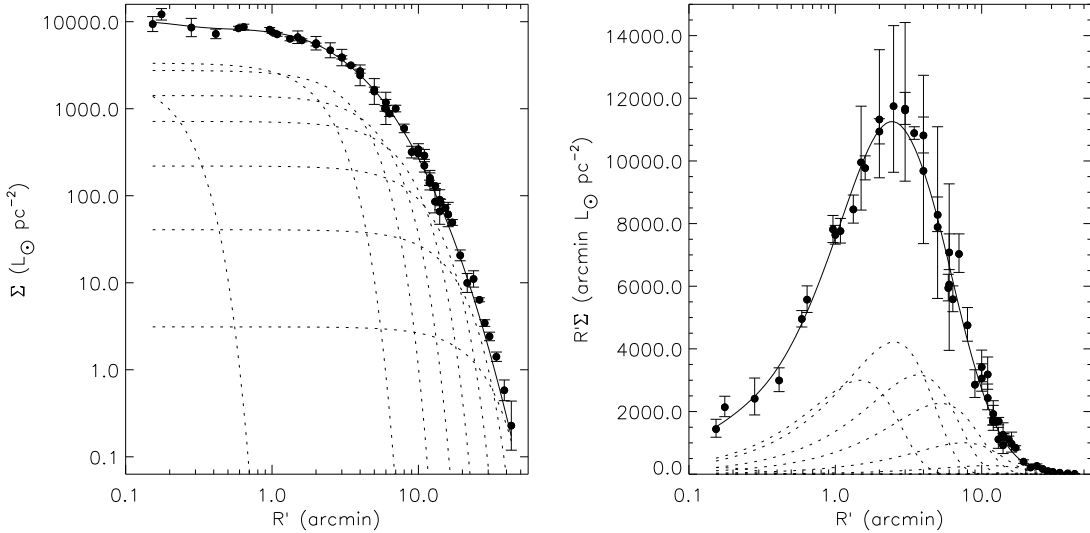
FIGURE 12 — *The Multi-Gaussian Expansion (MGE) of the V-band surface brightness profile of ω Cen. The filled circles represent the measurements by Meylan (1987), the dotted curves correspond to the eight Gaussians in the expansion and the solid curve represents their sum. The left panel shows the surface brightness Σ as a function of projected radius R' (in arcmin). Kalnajs (1999) has shown that the quantity $R'\Sigma$ in the right panel is a good diagnostic of the mass that is enclosed at each radius.*

7 DYNAMICAL MODELS FOR ω CEN

We use our method as described in § 5, to construct dynamical models for ω Cen. We obtain the mass model from a MGE-parameterization of the observed surface brightness. We compute the mean velocity and velocity dispersion of both proper motion components and along the line-of-sight in polar apertures on the plane of the sky. For a range of distances, inclinations and (constant) mass-to-light ratios, we then simultaneously fit axisymmetric Schwarzschild models to these observations. Additionally, we also allow for radial variation in the mass-to-light ratio.

7.1 MGE MASS MODEL

An MGE-fit is best obtained from a two-dimensional image, which gives direct information about the flattening and any radial variations in the two-dimensional structure of the object. Unfortunately, no such image is available to us, and the only published surface brightness observations of ω Cen consist of radial surface brightness profiles, and an ellipticity profile by Geyer et al. (1983). We therefore perform a one-dimensional MGE-fit to the radial surface brightness profile, and after that use the ellipticity profile to include flattening in the mass model.

We use the V-band surface brightness data from Meylan (1987), who combined various published measurements (Gascoigne & Burr 1956; Da Costa 1979; King et al. 1968). Their data consists of individual measurements along concentric rings, while the MGE-algorithm developed by Cappellari (2002) requires a regular (logarithmic) spacing of the surface brightness measurements. We therefore first describe the profile in terms of a fourth-order polynomial and then fit a set of one-dimensional

j	Σ_{0V}	σ'	q'
	$(L_\odot\,pc^{-2})$	(arcmin)	
1	2284.7077	0.15311	1.000000
2	3583.7901	1.47715	0.934102
3	3143.2029	2.52542	0.876713
4	1670.8477	3.69059	0.848062
5	840.86244	5.21905	0.849760
6	262.69433	7.53405	0.835647
7	46.995893	11.0685	0.866259
8	3.3583961	17.5470	0.926328

TABLE 2 — *The parameters of the 8 Gaussians from the MGE-fit to the V-band surface bright-ness profile of ω Cen as derived by Meylan (1987). The second column gives the central surface brightness (in $L_\odot\,pc^{-2}$) of each Gaussian component, the third column the dispersion (in ar-cmin) along the major axis and the fourth column the observed flattening.*

Gaussians to this polynomial. Eight Gaussians with different central surface bright-ness $\Sigma_{0V,j}$ and dispersion σ'_j are required by the MGE-fit (second and third column of Table 2). Fig. 12 shows that this MGE-model provides an excellent fit, not only to the surface brightness Σ, but also to $R'\Sigma$ (cf. Kalnajs 1999).

The MGE-parameterization is converted into a two-dimensional luminosity distri-bution by assigning an observed flattening q'_j to each Gaussian in the superposition. We take into account that the observed flattening of ω Cen varies as a function of radius (cf. Geyer et al. 1983). This is done by assuming that the flattening of the jth Gaussian q'_j is equal to the observed flattening at a projected radius $R' = \sigma'_j$. This is justified by the fact that a given Gaussian contributes most at radii close to its dispersion σ'_j. Although small deviations from the true two-dimensional light distri-bution in ω Cen may still occur, we showed in § 6.5 that this approximation does not significantly influence the derived intrinsic parameters for ω Cen. Moreover, a two-dimensional MGE-fit to the combination of the surface brightness profile from Meylan (1987) and the ellipticity profile from Geyer et al. (1983), yields nearly equivalent MGE parameters as those in Table 2, although the fit to the observed surface brightness profile is less good.

To conserve the total luminosity, we increase the central surface brightness of each Gaussian by $1/q'_j$. Taking into account a reddening of $E(B - V) = 0.11$ for ω Cen (Lub 2002), the total V-band luminosity of our mass model, at the canonical distance of 5.0 ± 0.2 kpc, is $L_V = 1.0 \pm 0.1 \times 10^6$ $L_\odot$. This compares well with other estimates of the total luminosity of ω Cen of 0.8×10^6 $L_\odot$ (Carraro & Lia 2000), 1.1×10^6 $L_\odot$ (Seitzer 1983) and 1.3×10^6 $L_\odot$ (Meylan 1987). The most flattened Gaussian in the superposition ($j = 7$) places a mathematical lower limit on the inclination of $33°$. This is safely below the constraint of 41–57 degrees found in § 4.5.

7.2   Mean velocity and velocity dispersion

We construct a polar aperture grid for the proper motions and line-of-sight velocities, as shown in Fig. 13. The dots in the left panel represent the positions, folded to the first quadrant, of the 2295 selected stars with ground-based proper motions. The overlayed polar grid, extending to about 20 arcmin, consists of 28 apertures.
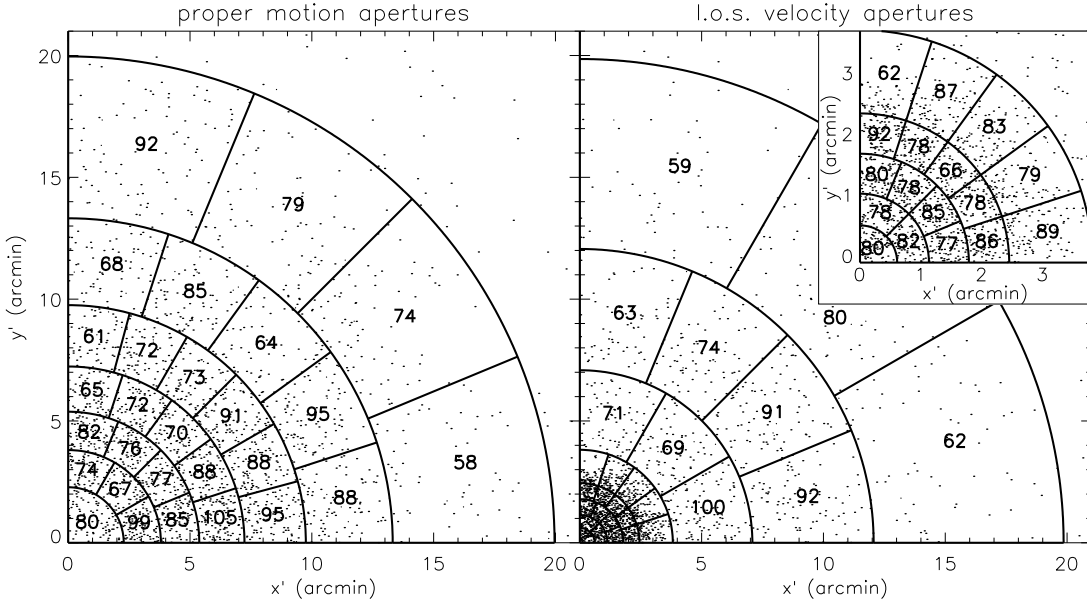
FIGURE 13 — *The polar aperture grid for the proper motions (left panel) and for the line-of-sight velocities (right panel). The dots represent the individual stars, with positions folded to the first quadrant, while the solid lines indicate the locations of the apertures. The number of stars included are indicated in each aperture. An enlargement of the inner part of the line-of-sight polar grid is shown in the top-right corner of the right panel.*

Per aperture, the number of stars is indicated, adding up to a total of 2223 stars. Similarly, the right panel shows the 2163 selected stars with line-of-sight velocities. The different number of stars and spatial distribution results in a polar grid of 27 apertures, which includes in total 2121 stars.

For each aperture, we use the maximum likelihood method (Appendix A) to compute the mean velocity V and velocity dispersion σ for both proper motion components on along the line-of-sight. We calculate corresponding errors by means of the Monte Carlo bootstrap method.

Each aperture contains around 50 to 100 stars. In Appendix B, we find that this is a good compromise between precision in the observables and spatial resolution. Including more stars per aperture by increasing its size decreases the uncertainties in the observables (and hence makes the resulting kinematic fields smoother). At the same time, since the apertures should not overlap to assure uncorrelated observables, this means less apertures in the polar grid and hence a loss in spatial resolution.

The properties of the apertures and corresponding mean kinematics are given in Table 3 for the proper motions and in Table 4 for the line-of-sight velocities. The mean velocity V_{observed} and velocity dispersion $\sigma_{\mathrm{observed}}$ fields are shown in the first and third column of Fig. 14 respectively. Although the average kinematics are only calculated in the first quadrant, we use the assumed axisymmetric geometry to unfold them to the other three quadrants to facilitate the visualization.
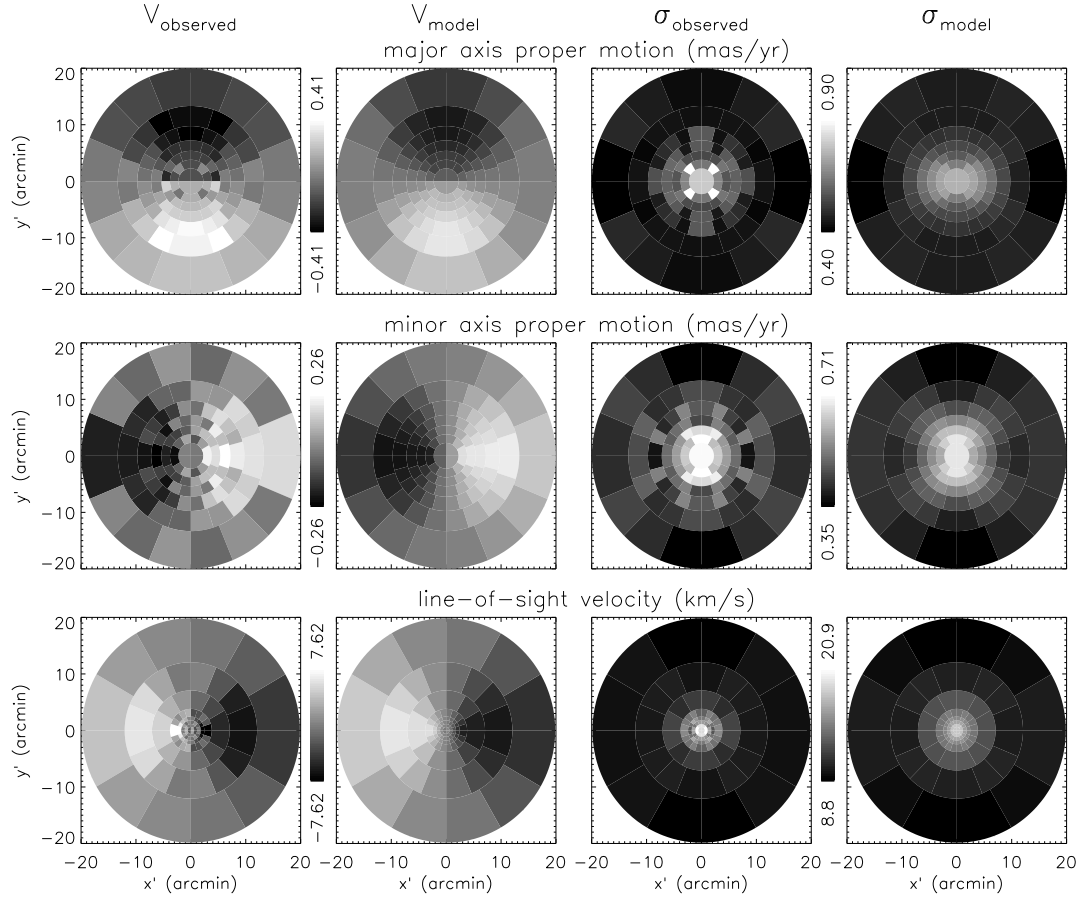
FIGURE 14 — *Mean velocity and velocity dispersion calculated from the observations of ω Cen (first and third column) and from the best-fit dynamical model with $D = 4.8$ kpc, $i = 50°$ and $M/L_V = 2.5$ M$_\odot$/L$_\odot$ (second and fourth column). The mean proper motion kinematics in the x'-direction (top row) and y'-direction (middle row), and the mean line-of-sight kinematics (bottom row), calculated in polar apertures in the first quadrant, are unfolded to the other three quadrants to facilitate the visualization.*

7.3   CONSTRUCTING DYNAMICAL MODELS

First, we calculate models for a range of values in distance D, inclination i and constant V-band mass-to-light ratio M/L_V. Next, fixing D and i at their measured best-fit values, we calculate a large set of models in which we allow M/L_V to vary with radius.

We sample the orbits on a grid of $21 \times 14 \times 7$ values in (E, L_z, I_3) on a radial range from 0.01 to 63 arcmin. This grid extends beyond the tidal radius of 45 arcmin (Trager et al. 1995), so that all mass is included. No PSF-convolution is used and the observables are stored directly onto the apertures.

We (linearly) sample D between 3.5 and 6.5 kpc in steps of 0.5 kpc, and additionally we refine the grid between 4.0 and 5.5 kpc to steps of 0.1 kpc. We vary i between 35 (close to the lower limit of 33 degrees imposed by the flattening, see § 7.1) and 90 degrees in steps of five degrees, and we refine between 40 and 50 degrees to steps of one degree. We choose the constant M/L_V values between 2.0 and 4.0 M$_\odot$/L$_\odot$ with steps 0.5 M$_\odot$/L$_\odot$, and we refine between 2.0 and 3.0 M$_\odot$/L$_\odot$ to steps of 0.1 M$_\odot$/L$_\odot$.

	$n_\star$	r_0	θ_0	Δr	$\Delta\theta$	$V_{x'}$	$\Delta V_{x'}$	$\sigma_{x'}$	$\Delta\sigma_{x'}$	$V_{y'}$	$\Delta V_{y'}$	$\sigma_{y'}$	$\Delta\sigma_{y'}$
1	80	1.14	45.0	2.28	90.0	-0.15	0.09	0.80	0.07	-0.01	0.09	0.70	0.05
2	99	3.04	15.0	1.53	30.0	-0.16	0.07	0.66	0.04	0.23	0.07	0.64	0.05
3	67	3.04	45.0	1.53	30.0	0.03	0.12	0.90	0.07	0.06	0.08	0.62	0.05
4	74	3.04	75.0	1.53	30.0	-0.15	0.08	0.64	0.07	-0.08	0.09	0.71	0.06
5	85	4.59	11.2	1.57	22.5	-0.27	0.06	0.57	0.03	0.19	0.06	0.57	0.05
6	77	4.59	33.7	1.57	22.5	-0.08	0.07	0.63	0.05	0.13	0.06	0.57	0.08
7	76	4.59	56.2	1.57	22.5	-0.20	0.07	0.55	0.05	0.13	0.08	0.69	0.06
8	82	4.59	78.7	1.57	22.5	-0.19	0.05	0.55	0.04	0.07	0.07	0.66	0.06
9	105	6.31	9.0	1.86	18.0	0.00	0.06	0.60	0.04	0.26	0.05	0.50	0.04
10	88	6.31	27.0	1.86	18.0	-0.13	0.07	0.61	0.04	0.13	0.05	0.48	0.05
11	70	6.31	45.0	1.86	18.0	-0.28	0.07	0.58	0.07	0.23	0.06	0.50	0.06
12	72	6.31	63.0	1.86	18.0	-0.25	0.05	0.45	0.04	-0.01	0.06	0.53	0.05
13	65	6.31	81.0	1.86	18.0	-0.25	0.07	0.58	0.05	0.05	0.06	0.45	0.03
14	95	8.49	7.5	2.52	15.0	-0.04	0.05	0.56	0.04	0.22	0.04	0.38	0.02
15	88	8.49	22.5	2.52	15.0	-0.09	0.05	0.46	0.04	0.10	0.07	0.53	0.07
16	91	8.49	37.5	2.52	15.0	-0.15	0.05	0.49	0.04	0.14	0.04	0.41	0.03
17	73	8.49	52.5	2.52	15.0	-0.31	0.06	0.51	0.06	0.19	0.05	0.44	0.03
18	72	8.49	67.5	2.52	15.0	-0.35	0.05	0.44	0.04	0.14	0.06	0.54	0.05
19	61	8.49	82.5	2.52	15.0	-0.40	0.07	0.58	0.05	-0.03	0.07	0.48	0.04
20	88	11.54	9.0	3.56	18.0	0.02	0.05	0.44	0.04	0.20	0.05	0.46	0.04
21	95	11.54	27.0	3.56	18.0	-0.17	0.04	0.42	0.04	0.17	0.05	0.49	0.04
22	64	11.54	45.0	3.56	18.0	-0.24	0.05	0.44	0.04	0.18	0.05	0.41	0.03
23	85	11.54	63.0	3.56	18.0	-0.41	0.05	0.44	0.03	0.05	0.04	0.43	0.03
24	68	11.54	81.0	3.56	18.0	-0.36	0.05	0.43	0.03	0.05	0.05	0.46	0.03
25	58	16.64	11.2	6.64	22.5	-0.02	0.06	0.40	0.04	0.19	0.06	0.41	0.05
26	74	16.64	33.7	6.64	22.5	-0.14	0.06	0.48	0.05	-0.01	0.06	0.45	0.04
27	79	16.64	56.2	6.64	22.5	-0.17	0.05	0.46	0.03	0.04	0.04	0.41	0.04
28	92	16.64	78.7	6.64	22.5	-0.21	0.05	0.43	0.03	-0.05	0.04	0.35	0.03

TABLE 3 — *The mean velocity and velocity dispersion calculated in polar apertures on the plane of sky from the proper motion observations. Per row the information per aperture is given. The first column labels the aperture and the second column gives the number of stars $n_\star$ that fall in the aperture. Columns 3–6 list the polar coordinates r (in arcmin) and the angle θ (in degrees) of the centroid of the aperture and the corresponding widths Δr (in arcmin) and $\Delta\theta$ (in degrees). The remaining columns present the average proper motion kinematics in units of $\mathrm{mas\,yr^{-1}}$. The mean velocity V with error ΔV and velocity dispersion σ with error $\Delta\sigma$ are given in columns 7–10 for the proper motion component in the x'-direction and in columns 11–14 for the proper motion component in the y'-direction.*

To investigate possible variation in M/L_V with radius, we make use of the eight Gaussian components of the MGE mass model (§ 7.1). In case of constant M/L_V, we obtain the intrinsic density by multiplying all the (deprojected) components with the same constant M/L_V value. To construct a mass model with a radial M/L_V profile, we multiply each component with its own M/L_V value, as in this way the calculation of the potential is still efficient. However, to reduce the number of free parameters (to make a search through parameter space feasible) and to enforce a continuous profile, we only vary the M/L_V values for the first, second, fourth and

	$n_\star$	r_0	θ_0	Δr	$\Delta\theta$	$V_{z'}$	$\Delta V_{z'}$	$\sigma_{z'}$	$\Delta\sigma_{z'}$
1	80	0.31	45.0	0.61	90.0	2.4	2.2	19.0	1.5
2	82	0.87	22.5	0.52	45.0	-3.1	2.1	20.9	1.4
3	78	0.87	67.5	0.52	45.0	0.2	1.9	19.5	1.4
4	77	1.46	11.2	0.66	22.5	0.0	1.9	16.7	1.3
5	85	1.46	33.7	0.66	22.5	-1.8	1.7	14.4	0.8
6	78	1.46	56.2	0.66	22.5	1.0	1.8	15.6	1.5
7	80	1.46	78.7	0.66	22.5	-0.7	1.7	16.2	1.2
8	86	2.12	9.0	0.66	18.0	-7.6	1.5	12.8	1.1
9	78	2.12	27.0	0.66	18.0	-6.4	1.6	14.3	0.8
10	66	2.12	45.0	0.66	18.0	-3.8	1.9	16.8	1.2
11	78	2.12	63.0	0.66	18.0	-3.0	1.7	15.9	1.0
12	92	2.12	81.0	0.66	18.0	-0.3	1.7	14.5	1.0
13	89	3.13	9.0	1.37	18.0	-7.6	1.6	15.3	1.0
14	79	3.13	27.0	1.37	18.0	-2.2	1.5	14.6	1.0
15	83	3.13	45.0	1.37	18.0	-1.0	1.4	14.1	0.8
16	87	3.13	63.0	1.37	18.0	-2.6	1.4	15.0	0.8
17	62	3.13	81.0	1.37	18.0	-2.9	1.9	13.4	1.3
18	100	5.45	15.0	3.27	30.0	-5.0	1.2	12.0	1.0
19	69	5.45	45.0	3.27	30.0	-3.1	1.3	10.9	1.1
20	71	5.45	75.0	3.27	30.0	-1.4	1.2	11.8	1.0
21	92	9.57	11.2	4.98	22.5	-6.2	1.0	10.0	0.9
22	91	9.57	33.7	4.98	22.5	-5.5	1.1	10.3	1.0
23	74	9.57	56.2	4.98	22.5	-2.4	1.2	10.3	0.9
24	63	9.57	78.7	4.98	22.5	0.2	1.3	9.8	0.9
25	62	15.96	15.0	7.80	30.0	-4.1	1.2	9.6	1.1
26	80	15.96	45.0	7.80	30.0	-1.9	1.2	9.8	0.7
27	59	15.96	75.0	7.80	30.0	-0.6	1.2	8.8	0.9

Table 4 — *The mean velocity and velocity dispersion calculated in polar apertures on the plane of sky from the line-of-sight velocity observations. Columns 1–6 are as in Table 3 and the remaining columns present the average line-of-sight kinematics in* $km\,s^{-1}$.

sixth component. For the third and fifth component, we interpolate between the M/L values of the neighboring components. To the outer two components we assign the same M/L_V value as the sixth component, because their individual M/L_V values are not well constrained due to the small number of kinematic measurements at these radii. With the distance and inclination fixed at their best-fit values from the case of constant mass-to-light ratio, we are left with a four-dimensional space to search through, requiring again a few days on (a cluster of) about 30 computers.

All dynamical models are fitted simultaneously to the two-dimensional light distribution of ω Cen (§ 7.1), and to the mean velocity and velocity dispersion of both proper motions components and along the line-of-sight, calculated in polar apertures on the plane of the sky (Fig. 14). Comparing the predicted values with the observations, results for each fitted model in a goodness-of-fit parameter χ^2, which we use to find the best-fit model and to determine the accuracy of the corresponding best-fit parameters.
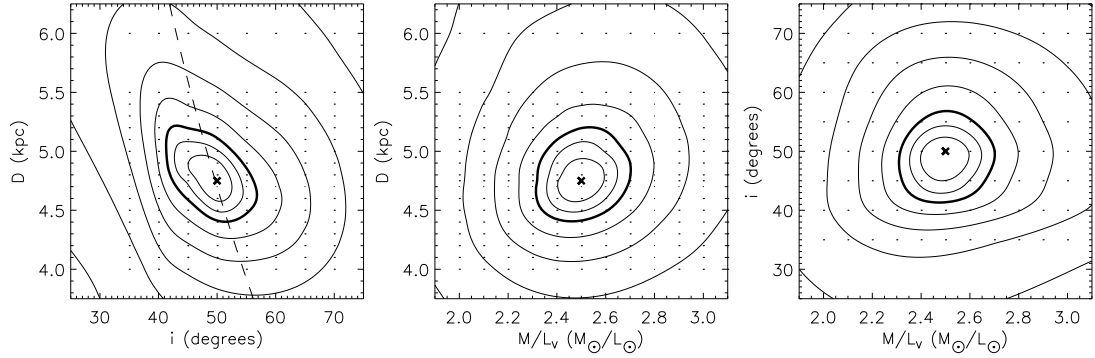
FIGURE 15 — *The (marginalized) goodness-of-fit parameter $\Delta\chi^2$ as a function of distance D, inclination i and mass-to-light ratio M/L_V, for different dynamical model fits (indicated by the dots) to the kinematics of ω Cen. The contours are as in Fig. 10. The best-fit dynamical model is at $D = 4.8$ kpc, $i = 50°$ and $M/L_V = 2.5$ M$_\odot$/L$_\odot$, indicated by the cross The dashed curve shows the $D\tan i = 5.6$ kpc constraint from the mean velocities (§ 4.5).*

8   BEST-FIT PARAMETERS

In Fig. 15, we show $\Delta\chi^2$ as a (marginalized) function of the distance D, inclination i and constant mass-to-light ratio M/L_V. The dots represent the values at which dynamical models have been constructed and fitted to the two-dimensional (photometric and kinematic) observations of ω Cen. The cross indicates the over-all best-fit model. The contours show that all three parameters are tightly constrained, with at the 68.3%-level (99.7%-level): $D = 4.8 \pm 0.3$ (± 0.5) kpc, $i = 50 \pm 3$ (± 5) degrees and $M/L_V = 2.5 \pm 0.1$ (± 0.2) M$_\odot$/L$_\odot$. As an illustration that our best-fit model indeed reproduces the observations, the mean velocity and velocity dispersion in polar apertures on the plane of the sky as they follow from this model are shown in respectively the second and fourth column of Fig. 14. The model fits the observations within the uncertainties given in Table 3 and 4.

After the discussion on the set of models where we allow the mass-to-light ratio M/L_V to vary with radius, we compare our best-fit values for the (constant) mass-to-light ratio, inclination and distance with results from previous studies.

8.1   MASS-TO-LIGHT RATIO VARIATION

Fig. 16 summarizes the results from fitting models in which we allowed the mass-to-light ratio M/L_V to vary with radius in the way described in § 7.3. The filled circles represent the eight Gaussian components, with the best-fit M/L_V value of each component plotted against their dispersions along the major axis (see column three of Table 2). The error bars represent the 68.3% confidence level.

The uncertainty on the innermost point around 0.15 arcmin is relatively large since at that small radius there are only a few observations (see Fig. 13) to constrain the M/L_V value. Nevertheless, the resulting M/L_V profile only shows a small variation, which is not significantly different from the best-fit constant M/L_V of 2.5 M$_\odot$/L$_\odot$.

In the above experiment, we fixed the distance and inclination at the best-fit values of $D = 4.8$ kpc and $i = 50°$ from the case of constant M/L_V. Although an important constraint is that all eight Gaussian components have to be at the same distance,
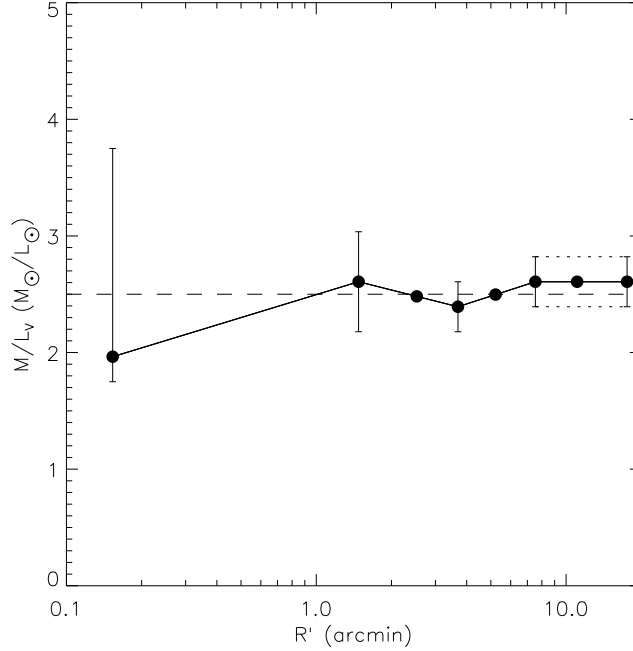
FIGURE 16 — *Variation in mass-to-light ratio M/L_V with projected radius R'. The filled circles represent the eight Gaussian components of the MGE mass model, with the best-fit M/L_V value of each component plotted against its dispersion along the major axis. With the distance and inclination fixed at $D = 4.8$ kpc and $i = 50$ degrees, we allowed variation in the M/L_V values for the four inner points with error bar, while the two outer points were shifted vertically similar to the fourth point, and the remaining two points were interpolated between the two neighboring points. Each of the models was simultaneously fitted to the photometric and kinematic observations of ω Cen. The error bars represent the 68.3% confidence level for the corresponding $\Delta\chi^2$-distribution with four degrees of freedom. The variation in the resulting M/L_V profile is small with no significant deviation from the best-fit constant M/L_V of 2.5 $M_\odot/L_\odot$ (horizontal dashed line).*

its precise value, as well as that of the inclination, is not crucial. We tested that a reasonable variation in these fixed values (within the 99.7% confidence level in Fig. 15) does not significantly change the best-fit M/L_V profile. We conclude that a constant mass-to-light ratio for ω Cen is a valid assumption.

8.2 MASS-TO-LIGHT RATIO

Our best-fit mass-to-light ratio of $M/L_V = 2.5 \pm 0.1$ $M_\odot/L_\odot$ lies in between the estimates by Seitzer (1983) of 2.3 $M_\odot/L_\odot$ and by Meylan (1987) of 2.9 $M_\odot/L_\odot$. Meylan et al. (1995) derived a value of 4.1 $M_\odot/L_\odot$, based on a spherical, radial anisotropic King-Michie dynamical model, while we find that ω Cen is flattened and outwards tangentially anisotropic (see § 9.2). Moreover, their adopted central value of the line-of-sight velocity dispersion is significantly higher than ours, even if we use the same data-set by M97.

Meylan et al. (1995) estimated the total mass of ω Cen to be 5.1×10^6 $M_\odot$, which is also significantly higher than what we derive. After multiplication with the total luminosity of our mass model of $L = 1.0 \times 10^6$ $L_\odot$ (at the best-fit distance of $D = 4.8 \pm 0.3$

kpc), we find a total mass of $M = (2.5 \pm 0.3) \times 10^6$ M$_\odot$. This is consistent with the value by Mandushev et al. (1991) of 2.4×10^6 M$_\odot$ and Seitzer (1983) of 2.8×10^6 M$_\odot$. The estimate by Meylan (1987) of 3.9×10^6 M$_\odot$ is higher, but again based on a spherical King-Michie model.

8.3 INCLINATION

The dashed curve in the left panel of Fig. 15 shows the $D \tan i = 5.6$ kpc constraint from the mean velocities derived in § 4.5. This constraint can be used to eliminate either the distance or the inclination and hence reduce the parameter space. Although we do not use this constraint in the dynamical models, it is clear that the above best-fit D and i yield $D \tan i = 5.6 \pm 0.2$ kpc, which is consistent with the value derived from the mean velocities.

The best-fit inclination of $i = 50 \pm 3$ degrees falls within the range of 30–60 degrees that was derived in Paper I from the amplitude of the proper motions, but is slightly higher than the estimate by van Leeuwen & Le Poole (2002) between 40 and 60 degrees. However, as discussed in § 4.5, they used models of modest complexity and freedom which require strong assumptions, whereas our method is more general and robust.

Our best-fit inclination implies that ω Cen is intrinsically even more non-spherical than the average observed flattening of $q' = 0.879 \pm 0.007$ (Geyer et al. 1983) already indicates. Using the relation $q^2 \sin^2 i = q'^2 - \cos^2 i$ for axisymmetric objects, we find an average intrinsic axial ratio $q = 0.78 \pm 0.03$.

8.4 DISTANCE

Adopting a reddening of $E(B - V) = 0.11$ for ω Cen (Lub 2002), the best-fit dynamical distance corresponds to a distance modulus of $(m - M)_V = 13.75 \pm 0.13$ (± 0.22 at the 99.7%-level). This is consistent with the (canonical) distance modulus of $(m - M)_V = 13.84$ by photometric methods, as given in the globular cluster catalog of Harris (1996), together with the uncertainty estimate of about 0.1 magnitude by Benedict et al. (2002), using the absolute magnitude of RR Lyrae stars. Using the infrared color versus surface brightness relation for the eclipsing binary OGLEC 17, Thompson et al. (2001) find a larger distance modulus of $(m-M)_V = 14.05 \pm 0.11$. However, their distance modulus estimates based on the measured bolometric luminosity of the binary components, are on average lower, ranging from 13.66 to 14.06.

Although our dynamical distance estimate is consistent with that by other methods, it is at the lower end. A lower value for the distance is expected if the proper motion dispersion is over-estimated and/or the line-of-sight velocity dispersion under-estimated (see also Appendix C, eq. C.1). As we saw in § 3, both are likely in the case of ω Cen if the kinematic data is not properly selected. The correction in § 4 for perspective rotation and especially for the residual solid-body rotation is crucial for the construction of a realistic dynamical model and a reliable distance estimate.

An impression of the effect of the selection and correction of the kinematic data on the distance estimate follows from the range of dynamical models we constructed for ω Cen. Before any selection and correction, the kinematics of the cluster stars give rise to a best-fit dynamical model at a distance as low as ~ 3.5 kpc. After removing from the proper motion data-set the stars disturbed by their neighbors, i.e., only selecting class 0 stars, the best-fit distance becomes ~ 4.0 kpc. The correction for perspective and solid-body rotation increase the best-fit distance to ~ 4.5 kpc. Fi-

nally, after the additional selection on velocity errors, we find our best-fit dynamical distance of 4.8 ± 0.3 kpc.

An even tighter selection does not significantly change the best-fit dynamical model and corresponding distance. The same is true if we use a different polar grid, with fewer or more stars per aperture, and if we restrict to only fitting the average kinematics in the inner or outer parts. Still, e.g. remaining interlopers in the proper motion data-set can cause a (small) under-estimation of the distance. Moreover, Platais et al. (2003) argue that possibly a (non-physical) residual proper motion color/magnitude dependence in the data-set of Paper I causes the systematic offset between the proper motions of the metal-rich RGB-a stars and those of the dominant HB and metal-poor RGB stars, noticed by Ferraro, Bellazzini & Pancino (2002). Since we do not correct for this possible systematic offset, the proper motion dispersion might be over-estimated and hence our distance estimate can be systematically too low. However, the effect is expected to be small since the number of RGB-a stars in the data-set is small. A deeper proper motion catalog, like that of King & Anderson 2002) obtained with the HST, is needed to better quantify (non-physical and physical) differences in the proper motions among the multiple stellar populations observed in ω Cen.

Although the distance and inclination are tightly linked through the mean velocities (§ 4.5), a small under-estimation of the distance only results in a slight over-estimation of the inclination (see also the solid curve in the right panel of Fig. 7). Similarly, the mass-to-light ratio is nearly insensitive to small changes in the distance.

9   INTRINSIC STRUCTURE

We use the intrinsic velocity moments of our best-fit dynamical model to investigate the importance of rotation and the degree of anisotropy in ω Cen. Additionally, the distribution of the orbital weights allows us to study the phase-space distribution function of ω Cen.

9.1   ROTATION

We calculate the intrinsic velocity moments of our best-fit model by combining the appropriate moments of the orbits that receive weight in the superposition. We consider the first and second order velocity moments, for which $\langle v_R \rangle = \langle v_\theta \rangle = \langle v_R v_\phi \rangle = \langle v_\theta v_\phi \rangle = 0$ because of axisymmetry. We define the radial, angular and azimuthal velocity dispersion respectively as $\sigma_R^2 = \langle v_R^2 \rangle$, $\sigma_\theta^2 = \langle v_\theta^2 \rangle$, $\sigma_\phi^2 = \langle v_\phi^2 \rangle - \langle v_\phi \rangle^2$. The only non-vanishing cross-term is $\sigma_{R\theta}^2 = \langle v_R v_\theta \rangle$. The average root-mean-square velocity dispersion σ_{RMS} is given by $\sigma_{\mathrm{RMS}}^2 = (\sigma_R^2 + \sigma_\theta^2 + \sigma_\phi^2)/3$.

A common way to establish the importance of rotation in elliptical galaxies and bulges of disk galaxies, is to determine their position in the $(V/\sigma, \epsilon)$-diagram (e.g., Davies et al. 1983). The *observational* quantities that are used for V, σ and ϵ are respectively the maximum (line-of-sight) velocity along the major axis, the average velocity dispersion within half the effective radius and the ellipticity at the effective radius. We obtain for ω Cen the observational quantities $V \sim 8$ km s^{-1} (at a radius of ~ 8 arcmin), $\sigma \sim 16$ km s^{-1} and $\epsilon \sim 0.15$ (Geyer et al. 1983). These values result in $(V/\sigma, \epsilon) \sim (0.5, 0.15)$, placing ω Cen just above the curve for isotropic oblate rotators.

On the other hand, the intrinsic velocity moments from our best-fit dynamical model for ω Cen, allow us to investigate *intrinsically* the importance of rotation. The grey scale in Fig. 17 show the ratio of the mean (azimuthal) rotation $\langle v_\phi \rangle$ over the
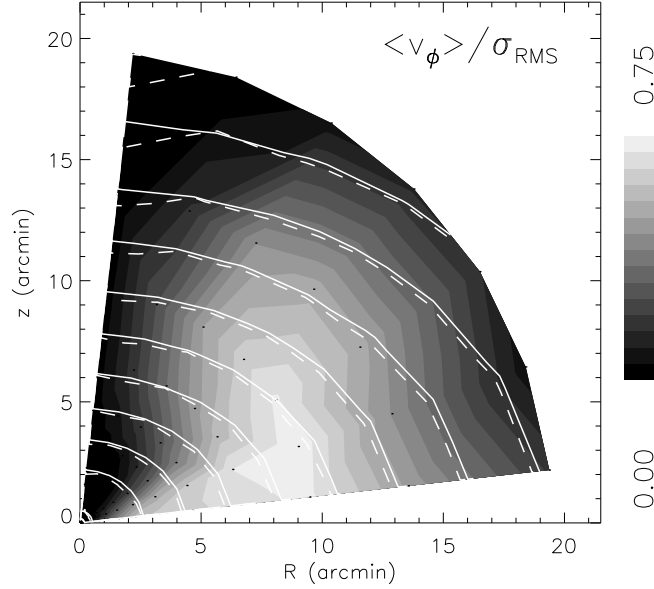
FIGURE 17 — *The grey scale represents the mean azimuthal rotation $\langle v_\phi \rangle$ in the meridional plane as a function of equatorial plane radius R and height z, and normalized by σ_{RMS} (excluding the axes to avoid numerical problems). The white curves are contours of constant mass density in steps of one magnitude, from the mass model (solid) and from the best-fit model (dashed), showing that the mass is well fitted. (See p. 250 for a color version of this figure.)*

average root-mean-square velocity dispersion σ_{RMS}, as function of the position in the meridional plane. Near the equatorial plane and between radii of about 5 to 15 arcmin, this ratio is > 0.5. The maximum of ~ 0.7 around 8 arcmin coincides with the peak in the mean line-of-sight velocity field. Within this region in the meridional plane rotational support is important. However, more inwards and further outwards this ratio rapidly drops below 0.5 and ω Cen is at least partly pressure supported. We conclude that rotation is important in ω Cen, but it is not a simple isotropic oblate rotator.

9.2 ANISOTROPY

For the velocity distribution in ω Cen to be isotropic all three velocity dispersion components σ_R, σ_θ and σ_ϕ have to be equal and the cross-term $\sigma_{R\theta}$ has to vanish. Fig. 18 shows that this is not the case.

In the top panels, we show the degree of anisotropy in the meridional plane. The top-left panel shows the radial over the angular velocity dispersion σ_R/σ_θ. This ratio does however not include the non-zero cross-term $\sigma_{R\theta}$. The latter causes the velocity ellipsoid to be rotated with respect to the R and θ coordinates. Taking this into account the semi-axis lengths of the velocity ellipsoid in the meridional plane are given by $\sigma_\pm^2 = (\sigma_R^2 + \sigma_\theta^2)/2 \pm \sqrt{(\sigma_R^2 - \sigma_\theta^2)^2/4 + \sigma_{R\theta}^4}$. In the top-right panel, we show the ratio of this minor σ_- and major σ_+ semi-axis length of the velocity ellipsoid (which is by definition in the range from zero to unity). This demonstrates that the velocity distribution of ω Cen is nearly isotropic near the equatorial plane, but becomes increasingly
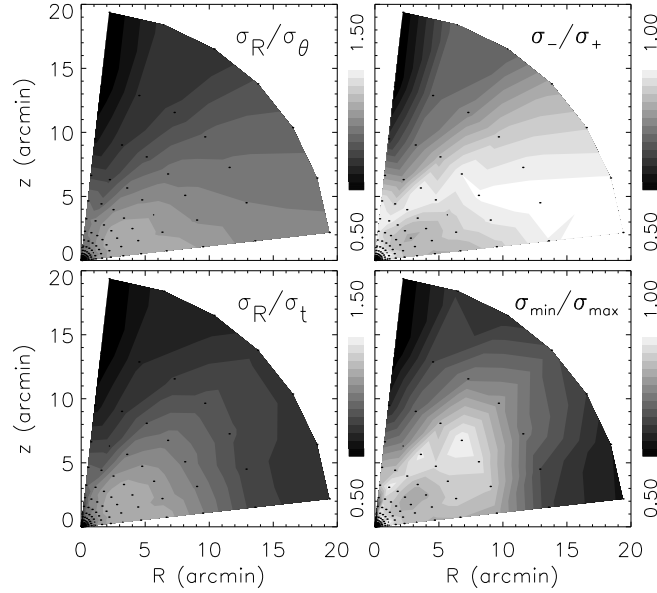
FIGURE 18 — *Degree of anisotropy as function of the equatorial plane radius R and height z (excluding the axes to avoid numerical problems). The top panels show the degree of anisotropy in the meridional plane: left the radial over the angular velocity dispersion and right the minor σ_- over the major σ_+ semi-axis length of the velocity ellipsoid, taking into account the cross-term $\sigma_{R\theta}$. The bottom panels include the azimuthal velocity dispersion: left the radial over the tangential velocity dispersion, with $\sigma_t^2 = (\sigma_\theta^2 + \sigma_\phi^2)/2$, and right the minimum over the maximum of the three semi-axis lengths σ_+, σ_- and σ_ϕ of the velocity ellipsoid. See text for further details.*

tangential anisotropic towards the symmetry axis.

In the bottom panels we also include the azimuthal velocity dispersion σ_ϕ. The bottom-left panel shows the radial over the tangential velocity dispersion, where the latter is defined as $\sigma_t^2 = (\sigma_\theta^2 + \sigma_\phi^2)/2$. Again this ratio does not take into account the cross-term $\sigma_{R\theta}$. The actual degree of anisotropy is given by the three semi-axis lengths σ_+, σ_- and σ_ϕ of the velocity ellipsoid. In the bottom-right panel, we show, as a function of the position in the meridional plane, the minimum over the maximum of these three semi-axis lengths. Except for the region near the equatorial plane and within 10 arcmin, the best-fit model for ω Cen is clearly not isotropic. Even within this region, between about 3 and 5 arcmin, it is (slightly) radially anisotropic. Outside this region ω Cen becomes increasingly tangentially anisotropic.

Clearly, isotropic models are not suitable to model ω Cen. Also dynamical models with a two-integral distribution function of the form $F(E, L_z)$, with $L_z = R\langle v_\phi \rangle$ the angular momentum component along the symmetry z-axis, are not able to describe the complex dynamical structure of ω Cen. For these models the solution of the Jeans equations can be used to construct dynamical models in a straightforward way (e.g., Satoh 1980; Binney, Davies & Illingworth 1990) and they allow for azimuthal anisotropy. However, for these models $\sigma_R = \sigma_\theta$ and $\sigma_{R\theta} = 0$, i.e., isotropy in the full meridional plane, which is not the case for ω Cen (top panels of Fig. 18). Our axisymmetric dynamical models do not have these restrictions as they are based on a
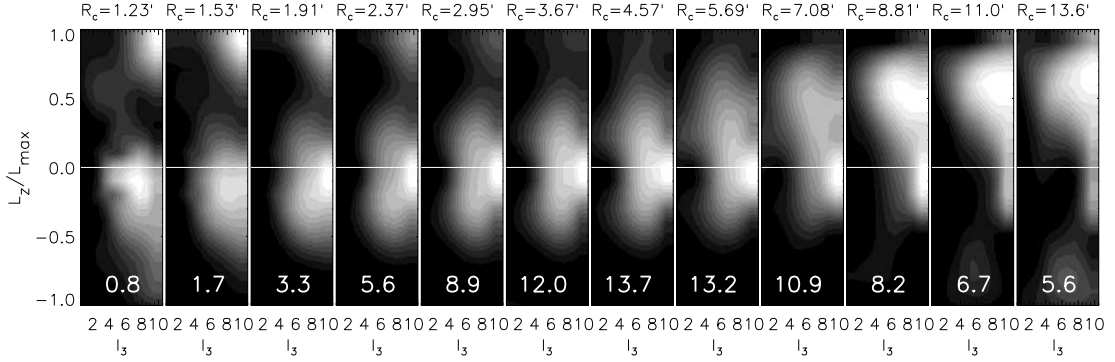
FIGURE 19 — *The orbital weight distribution for our best-fit model of ω Cen. From left to right, the panels show the orbital weight distribution at increasing distance from the center, which corresponds to increasing energy. The radius R_c (in arcmin) of the circular orbit at the corresponding energy is given above each panel. The radial range that is shown is constrained by the observations and contains more than 90% of the total cluster mass. The vertical axis represents the angular momentum L_z in units of L_{max}, the angular momentum of the circular orbit. The horizontal axis represents the third integral I_3, parameterized by the number of the (linearly sampled) starting angle of the orbit. Black shading corresponds to zero orbital weights, and white corresponds to the maximum orbital weight in each panel. At the bottom of each panel the fraction (in %) of the included mass with respect to the total mass is indicated. (See p. 250 for a color version of this figure.)*

general three-integral distribution function $F(E, L_z, I_3)$, which we investigate next for our best-fit model.

9.3 DISTRIBUTION FUNCTION

Each orbit in our models is characterized by the three integrals of motion E, L_z and I_3. As function of these three integrals, we show in Fig. 19 for our best-fit model of ω Cen the distribution of the (mass) weights that were assigned to the different orbits in the NNLS-fit. The energy E is sampled through the radius R_c (in arcmin) of the circular orbit (different panels), of which we show the range that is constrained by the observations and that contains more than 90% of the total cluster mass. The angular momentum L_z (vertical) is in units of L_{max}, the angular momentum of the circular orbit. The third integral I_3 (horizontal) is parameterized by the linearly sampled starting angle of the orbit, from the equatorial plane towards the symmetry axis, and of which the number is given.

In each panel, the orbital weights are scaled with respect to the maximum orbital weight in that panel, indicated by the white color, whereas black corresponds to zero orbital weight. The fraction of the sum of the mass weights in each panel with respect to total mass in all panels is given at the bottom of each panel (in %). To avoid an unrealistic orbital weight distribution that fluctuates rapidly for adjacent orbits, we regularize our models (§ 5.4). For values of the smoothening parameter below $\Delta = 4$ and even without regularization, we find the same best-fit parameters and although the distribution function becomes spiky, the main features of Fig. 19 remain.

Most of the mass in the orbital weight distribution is in the component that is prominent in all panels. With increasing radius, the average angular momentum L_z of this component increases from nearly zero to a significant (positive) value in

the outer parts. This reflects the outwards increasing tangential anisotropy already seen in the bottom-left panel of Fig. 18. An almost non-rotating part is still present beyond 5 arcmin, attached to the rotating component, which becomes the dominant component (in mass). There is also a separate component at $L_z/L_{\max} \sim 1$ that is clearly visible between about 1 and 3 arcmin. Within this radial range, this maximum rotating component contributes almost 20% of the mass, and it includes about 4% of the total mass, i.e., its mass is of the order of 10^5 M$_\odot$.

In the right-most panels of Fig. 19 there is a (weak) signature of a component with $L_z/L_{\max} \sim -1$, which we expect to be a spurious feature due to insufficient observational constraints. Whereas (nearly) circular orbits ($|L_z|/L_{\max} \sim 1$) are confined in radius to R_c, orbits with lower $|L_z|$ can go further inwards, so that they have most of their contribution (their cusps) at a smaller radius than R_c (e.g., Cappellari et al. 2004). Hence, the apparent feature at $L_z/L_{\max} \sim -1$ in the most-right panel is only constrained by data around and beyond the radius $R_c = 13.6$ arcmin, where the coverage of the data is sparse with only a few polar bins (see Fig. 13). The main component in this panel at $L_z/L_{\max} \sim 0.5$ is (mostly) constrained by data at smaller radii, where there is good data coverage. The separate maximum rotating component between 1 and 3 arcmin is constrained by only a few proper motion apertures, but is strongly constrained by the line-of-sight velocity data.

Due to the difference in spatial coverage between the proper motion and line-of-sight velocity data, the two data-sets (better) constrain different parts of the orbital weight distribution. By fitting besides the light distribution of ω Cen the mean velocity and velocity dispersion of only the proper motion components, we find a less prominent separate component between 1 and 3 arcmin, but it is still present. In the case of only fitting the mean line-of-sight velocity and velocity dispersion, this separate component is clearly visible and even extends into the outer rotating main component. The transition between the main non-rotating and rotating component is in the case of only line-of-sight data more abrupt than in Fig. 19. However, the proper motion data, which has a better coverage in the outer parts, shows a similar smooth transition. We conclude that, although the spatial coverage is different, both data-sets give rise to the same main features in the orbital weight distribution.

9.4 DYNAMICAL SUBSTRUCTURES

Within 5 arcmin the main component has on average a high value of I_3. In combination with the low value of L_z, we interpret this as a non-rotating spheroidal structure. Beyond 5 arcmin, L_z increases and I_3 decreases, and the main component flattens and rotates faster. The smaller component attached to it may well be the signature of the fading non-rotating spheroidal component.

For the separate component between 1 and 3 arcmin, L_z approaches its maximum value. As a result, the zero-velocity curve shrinks towards the circular orbit in the equatorial plane, and the corresponding orbits are all flat, irrespective of the (high) value of I_3 (see also Fig. 3 of Cretton et al. 1999). Hence, this fast-rotating component is likely to be an inner disk, which fades away into the more massive main rotating component at larger radius.

We compute the spatial distribution and average kinematics of these possible substructures in the phase-space of ω Cen. To this end we select the orbits from our best-fit model that contribute non-zero weight to three different parts of the distribution function in Fig. 19. We select the *inner* main component in the 7 left-most panels,
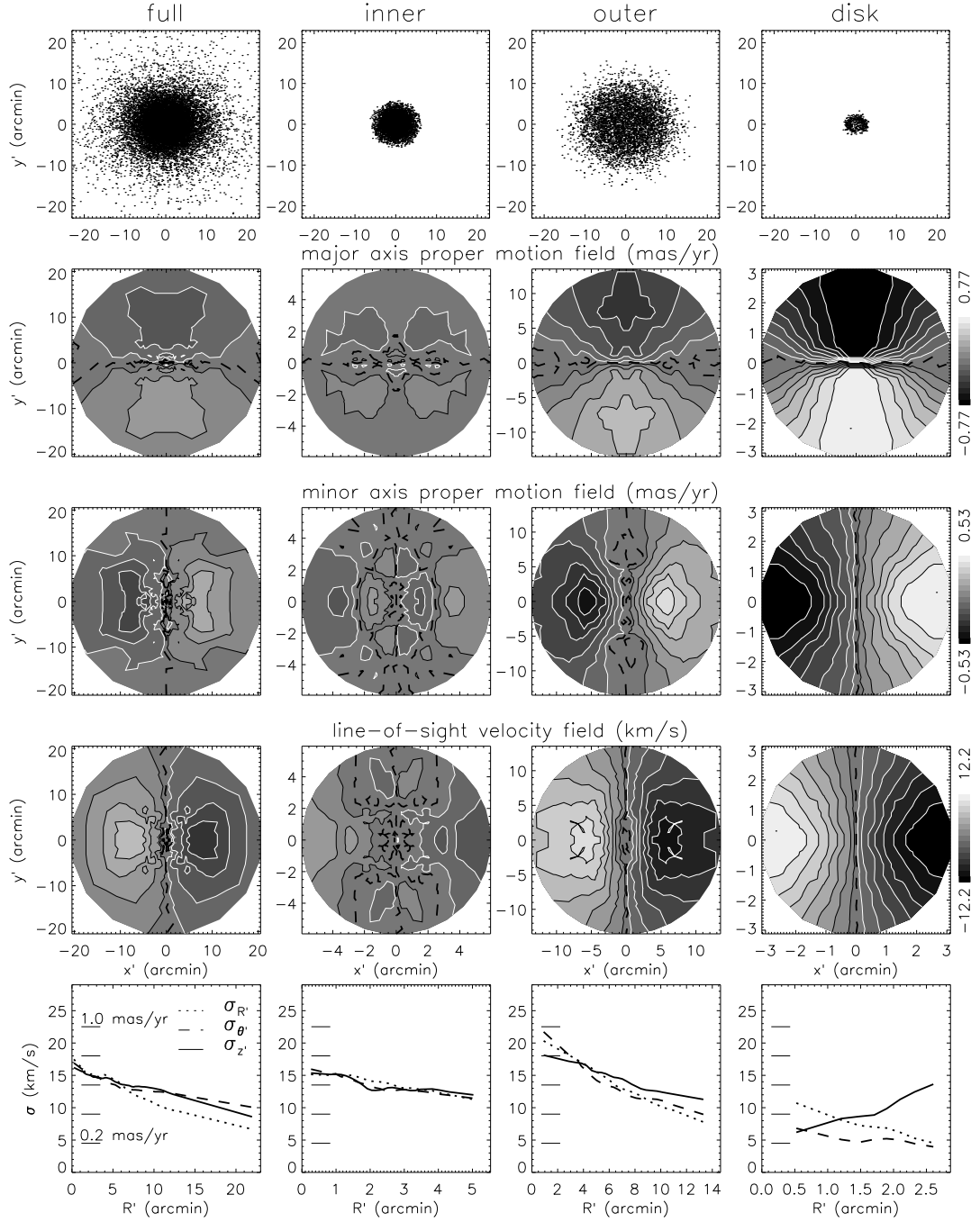
FIGURE 20 — *Kinematics of different components in the distribution function of our best-fit model for ω Cen. From left to right: full distribution function, main inner component, main outer component and separate disk component between 1 and 3 arcmin (see text for details). From top to bottom: spatial distribution, mean velocity fields in the direction of the major x'-axis, the minor y'-axis and the line-of-sight z'-axis, and mean velocity dispersion profiles. The radial dispersion $\sigma_{R'}$ (dotted) and tangential dispersion $\sigma_{\theta'}$ (dashed) are on the plane of the sky and $\sigma_{z'}$ (solid) is the line-of-sight dispersion. (See p. 251 for a color version of this figure.)*

excluding the separate *disk* component in the 5 left-most panels, and the *outer* main component in the 3 right-most panels (excluding the weak feature in the bottom). For each orbit with non-zero weight, we then randomly draw points along its numerically integrated orbit, with the number of drawings proportional to its relative weight. In this way, we make an (N-body) realization of our best-fit model consisting of a couple of tens of thousands of particles, representing the stars in ω Cen. For each of these stars, we determine the position on the plane of the sky and the three velocity components; the two proper motion components in the plane of the sky and the line-of-sight velocity. For the stars that belong to a certain part or substructure of phase-space, we then calculate the spatial distribution and mean kinematics.

Fig. 20 shows the results for all stars, those in the inner and outer main component and those in the separate disk component, respectively, per column from left to right. The first row shows the spatial distribution. The flattening of the spatial distribution of all stars and of the outer main component are both about 0.88, similar to the average observed flattening for ω Cen. The inner main component, going out to a radius of about 6 arcmin, is rounder with a flattening of about 0.94. The spatial distribution of the disk component only extends to a radius of about 3 arcmin, has an average flattening as lows as 0.60 and is less dense in the center as this maximum rotating disk consists of stars on (nearly) circular orbits which avoid the center. The second to fourth row show the mean velocity fields in respectively the direction of the major x'-axis and the minor y'-axis on the plane of the sky and the line-of-sight z'-axis. In each panel the axes are scaled with respect to the spatial extent of each component. Whereas the inner main component indeed hardly shows any rotation, the outer main component clearly rotates and the separate disk component rotates even faster. In the last row, the velocity dispersion profiles are presented, radial (dotted) and tangential (dashed) on the plane of the sky and along the line-of-sight (solid). Even though the outer main component is flatter and rotates faster than the inner main component, it is not kinematically colder due to the mixture of orbits with different L_z values. On the other hand, the maximum rotating disk is the kinematically coldest component. Whereas the inner main component is nearly isotropic, the outer main component is anisotropic and the disk component is even stronger anisotropic.

The presence of dynamical substructures implies that the formation history of ω Cen is more complicated than expected for a typical globular cluster. However, the interpretation of these different components in the distribution function is very difficult. In what follows we investigate the possible effects due to the tidal interaction between ω Cen and the Milky Way (§ 9.5), and the possible link to the observed multiple stellar populations in ω Cen (§ 9.6).

9.5   TIDAL INTERACTION

Based on its current position and motion in the Milky Way (MW), Dinescu, Girard & van Altena (1999) simulated the orbit of ω Cen around the Galactic Center (GC). They found that the average orbit is inclined by only $17°$ with respect to the Galactic plane, has a period of $P \sim 122$ Myr and an angular momentum of about 406 kpc km s^{-1}. Assuming that the average orbit of ω Cen is circular, we thus find a radius $R_{OC} \sim 2.8$ kpc and a velocity of about 143 km s^{-1}, of which the component perpendicular to Galactic plane $v_\perp \sim 42$ km s^{-1}. Since the scale height of the MW disk is typically 250 pc, it takes about $t_{enc} \sim 12$ Myr for ω Cen to cross the MW disk. This means that for nearly 10% of its time ω Cen is immersed in the disk and feels the additional
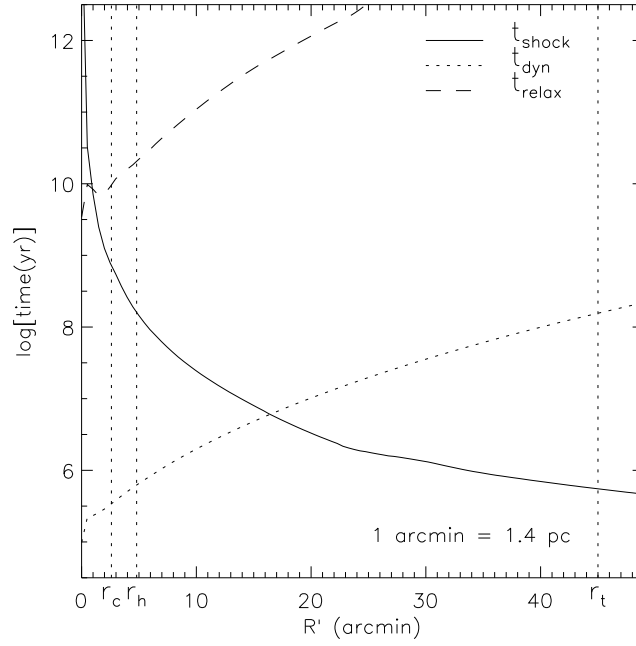
FIGURE 21 — *Timescales as function of the projected radius R'. The solid curve represents the timescale on which shocks, caused by successive passages of ω Cen through the MW disk, change the mean-squared velocity of a cluster star by the order of the (local) velocity dispersion of the cluster. The dotted and dashed curves show respectively the dynamical time t_{dyn} and relaxation time t_{relax}. The vertical dashed lines indicate with increasing distance the core radius r_t, the half-light radius r_h and the tidal radius r_t of ω Cen.*

gravitational field.

To investigate what effect the MW tidal field has on the stars in ω Cen, we use the impulse approximation as described by Binney & Tremaine (1987, p. 446), with the typical properties of the MW from their Tables 1-1 and 1-2. We assume a Cartesian coordinate system with its origin at the center of ω Cen and the z-axis perpendicular to the MW disk. If ω Cen goes through the MW disk, the effect on the velocity component perpendicular to the disk is the largest. Hence, the velocity of a cluster star changes on average by $|\Delta v| \sim z|g_z(R)|/v_\perp$, where g_z is the z-component of the gravitational field of the MW disk. The cumulative effect of successive passages through the MW disk becomes of the order of the (local) velocity dispersion σ of the cluster on a timescale of $t_{\mathrm{shock}} \sim P\sigma^2 v_\perp^2/(8z^2 g_z^2)$.

An infinite disk with surface density Σ generates a gravitational field $g_z = 2\pi G\Sigma$. In the solar neighborhood the MW disk has a surface density of $\Sigma_\odot \sim 75 \ \mathrm{M_\odot \, pc^{-2}}$. Assuming that the MW disk falls off as $\exp(-R/R_d)$ in the radial coordinate, with $R_d = 3.5$ kpc , we find that at the mean circular radius $R = R_{\mathrm{OC}}$ of ω Cen's orbit around the GC, $g_z \sim 2.9 \times 10^{-13} \ \mathrm{km\,s^{-2}}$. For a spherical shell of stars of radius r, we have that on average $z^2 = r^2/3$. We thus find that the timescale on which disk shocking becomes important is

$$t_{\mathrm{shock}} \sim 21 \left(\frac{\sigma}{\mathrm{km\,s^{-1}}}\right)^2 \left(\frac{r}{\mathrm{arcmin}}\right)^{-2} \quad \mathrm{Myr}. \tag{9.1}$$

Fig. 21 shows t_{shock} (solid curve) as function of the projected radius R' (in arcmin). We used the line-of-sight velocity dispersion as given in Fig. 8, smoothed and extrapolated to larger radii using measurements by Scarpa, Marconi & Gilmozzi (2003) between about 20 and 30 arcmin[8]. In the same figure we have also plotted the dynamical time t_{dyn} (dotted curve; Binney & Tremaine 1987, eq. 2-30) and the relaxation time t_{relax} (dashed curve; Spitzer & Hart 1971; Binney & Tremaine 1987, eq. 8-71). The three vertical dashed lines indicate respectively the core radius $r_c = 2.6$ arcmin, the half-light radius $r_h = 4.8$ arcmin and the the tidal radius $r_t = 45$ arcmin (e.g., Trager et al. 1995).

Clearly, the impulse approximation is not valid near the center of ω Cen, where the period of the stellar orbits $T \equiv 4\,t_{\mathrm{dyn}}$ is much smaller than the duration of the passage through the disk $t_{\mathrm{enc}} \sim 12$ Myr. Disk shocking is thus unimportant at the center of ω Cen: the orbits evolve adiabatically and emerge unharmed from the encounter. Around a radius of 16 arcmin, where T is about twice t_{enc}, disk shocks begin to play an important role since the disk shocking time becomes of the order of the dynamical time $t_{\mathrm{shock}} \sim t_{\mathrm{dyn}} \sim 6$ Myr. At the tidal radius of 45 arcmin, the MW disk gravitational field becomes dominant.

The effect that the MW tidal field has on the internal dynamics of ω Cen also strongly depends on the relative orientation and spinning direction of the angular momentum vector of the stars in ω Cen (internal) and the angular momentum vector of its orbit around the GC (external). We found that the rotation axis is about $50°$ inclined with respect the line-of-sight (the z'-axis) in the direction South[9]. On the plane of sky, the rotation axis projects onto the minor y'-axis, which makes an angle of about $10°$ away from North in the direction East. The equatorial coordinates of ω Cen are $\alpha_0 = 13^h 26^m 46^s$ and $\delta_0 = -47°28'43''$ (J2000), which correspond to a Galactic longitude and latitude of $l = 309°$ and $b = 15°$. Hence, the rotation axis is nearly parallel (angle $< 3°$) to the equatorial plane, and makes an angle of about $65°$ with respect to the Galactic plane. Seen from the North Galactic pole, ω Cen is moving in anti-clockwise direction around the GC. The rotation inside ω Cen is dominated by orbits with positive L_z values in Fig. 19, which correspond to clockwise rotation.

We thus find that the internal and external angular momentum vector are for more than 90% parallel with respect to each other with opposite spinning direction. From mergers of spinning galaxies it is well known that if the spins are anti-parallel as in this case, the orbital disruption is much less than in the case of parallel spins (e.g., Toomre & Toomre 1972). Hence, in the past ω Cen might have contained a significant number of stars on orbits with negative L_z (parallel spin), which then were removed from the cluster during its successive passages through the MW disk. Stars on orbits with positive L_z (anti-parallel spin) had a bigger chance to survive.

Furthermore, the stars on more radial orbits (those with smaller values of L_z) cover a broader range in radius, with the influence of the MW tidal field becoming stronger at increasing radius. In the course of time, these radial orbits thus have a bigger chance of being disrupted than the more tangential orbits with similar mean radius.

---

[8]Taking into account the measurement error of about 1 km s^{-1} and the perspective rotation that can be as large as 1.5 km s^{-1} at those radii (eq. 4.1).

[9]This means that in the common definition of the inclination, as in eq. (2.2), the best-fit inclination is -50°. This also explains the sign difference of $\langle v_{z'} \rangle$ in eq. (4.3) and along the vertical axis of the plot in the middle panel of Fig. 7. However, we decided to adopt the usual convention to take the value for the inclination in the range from $0°$ (face-on) to $90°$ (edge-on).

Both effects (together) might explain the prominent rotating main component in the distribution function in Fig. 19 beyond a radius of 10 arcmin, while the non-rotating main component that dominates inwards, fades away. The removal of the more radial orbits also naturally explains the outwards increasing tangential anisotropy in our best-fit model of ω Cen (§ 9.2).

The above analysis shows that the frequent passages of ω Cen through the MW disk most likely have played a crucial role in the evolution of this cluster. At least part of the phase-space structure of ω Cen may well be caused by the tidal field of the MW. Detailed (N-body) simulations are needed to further quantify this.

9.6 MULTIPLE STELLAR POPULATIONS

Among the Galactic globular clusters, ω Cen especially stands out because of its chemical inhomogeneity, first revealed in photometric investigations by Dickens & Woolley (1967) and spectroscopically confirmed by Freeman & Rodgers (1975). Besides the main population of metal-poor stars ($\sim 65\%$ of all stars with [Ca/H]~ -1.4) and an intermediate population ($\sim 30\%$, [Ca/H]~ -1.0), recently also a separate metal-rich population ($\sim 5\%$, [Ca/H]~ -0.5) has been identified (Lee et al. 1999; Pancino et al. 2000), and even the main sequence of ω Cen is bifurcated (Bedin et al. 2004).

Theses different stellar populations also appear to have a different spatial distribution. Whereas the metal-poor stars seems to follow the observed flattening of ω Cen in the East-West direction, the more metal-rich stars are elongated in the North-South direction and also more centrally concentrated (e.g., Pancino et al. 2003). There are also indications of differences in the kinematics of the stellar populations. Norris et al. (1997) find that the metal-poor populations have on average a higher line-of-sight velocity dispersion and exhibit a well-defined line-of-sight rotation, while the metal-rich populations show no significant rotation. Ferraro et al. (2002) claim that the separate metal-rich population has a coherent bulk proper motion significantly different from the other cluster stars.

We use the empirical relation in eq. (15) of Paper I to estimate the [Ca/H] abundances of stars in our analysis with V-band magnitude and $B-V$ color measurements consistent with the top of the red giant branch ($V < 13.5$ and $B - V > 0.7$). The resulting [Ca/H] histograms for the proper motion and line-of-sight velocity stars both show a distribution with a broad peak around [Ca/H]~ -1.2 and a long tail extending beyond [Ca/H]~ -0.5. In both cases the peak shows a small dip, so that we might divide the stars into a metal-poor population with [Ca/H]≤ -1.2 and a metal-rich population with [Ca/H]> -1.2, similar to Norris et al. (1997).

Comparing the mean line-of-sight kinematics of the metal-poor and metal-rich stars, we confirm the result of Norris et al. (1997) that the more centrally concentrated metal-rich stars are on *average* kinematically cooler and nearly non-rotating. The line-of-sight velocity dispersion *profile* is steeper for the metal-richer stars than for the metal-poor stars, such that that in the center the metal-richer stars are even (slightly) kinematically warmer. The proper motions seems to imply a similar difference in the slope of the velocity dispersion profiles. However, with the proper motion errors on average four times larger than those of the line-of-sight velocities (see also Fig. 8), there are no significant differences between the kinematics of the metal-poor and metal-rich stellar populations.

The above correlations between the kinematics and chemical properties of stars in ω Cen, are expected to show up in the distribution function (see also Freeman

2002). The centrally concentrated non-rotating metal-rich stars would lie near the bottom of the potential well at the lower values of E found in the cluster, symmetrically distributed over positive and negative values of L_z, and towards higher values of I_3. The rotating metal-poor stars would span the entire range of E, with an asymmetric distribution in L_z and towards lower I_3.

These expectations are consistent with the orbital weight distribution of our best-fit dynamical model of ω Cen (Fig. 19 and 20). Whereas the metal-richer stars might well be associated with the inner non-rotating part of the main component, we might see the kinematical signatures of the metal-poorer stars becoming dominant when the main component flattens and rotates faster in the outer parts. Still, we have to be careful as these are (indirect) indications of a link between substructures in the distribution function and the different stellar populations.

To investigate directly the distribution function of the different stellar populations, once can try to construct separate dynamical (Schwarzschild) models. However, since the separation into different stellar populations is not evident, separate mass models are needed and the separate kinematic constraints are based on much fewer stars, this is very difficult with the current data-set. A more feasible approach is to model together, in a consistent way, the observed kinematics and physical properties of the stars. For example, by labeling the orbits in the model with different colors, the observed color (averaged per aperture) can be used to constrain the model in addition to the photometry and kinematics. On the other hand, now that we have constrained the global parameters (distance, inclination and mass-to-light ratio) considerably, it has become feasible to use non-linear maximum likelihood techniques to directly incorporate discrete stellar measurements. In this way, for the model that best fits (simultaneously) the measured kinematics and age and metallicity indicators of individual stars, the different stellar populations can be cleanly separated in phase-space. This extension, which we leave for a future paper, will provide an important contribution to solving the stellar population puzzle in ω Cen, and clarify its formation history.

10 CONCLUSIONS

We used an extension of Schwarzschild's (1979) orbit superposition method to construct realistic axisymmetric dynamical models for ω Cen with an arbitrary anisotropic velocity distribution. By fitting these models simultaneously to proper motion and line-of-sight velocity measurements, we measured the radial mass-to-light profile, the inclination and the distance to ω Cen, which is needed to convert the proper motions to physical units. This dynamical distance estimate can provide a useful calibration for the photometric distance ladder.

We used the ground-based proper motions from Paper I and the line-of-sight velocities from four independent data-sets. We brought the kinematic measurements onto a common coordinate system and carefully selected on cluster membership and on measurement error. This provided a homogeneous data-set of 2295 stars with proper motions accurate to 0.20 mas yr^{-1} and 2163 stars with line-of-sight velocities accurate to 2 km s^{-1}, covering a radial range out to about half the tidal radius of the cluster. We corrected the kinematic measurements for perspective rotation and removed a residual solid-body rotation component in the proper motions. We showed that the latter can be measured without any modeling other than assuming axisymmetry and at the same time we obtained a tight constraint on $D \tan i$ of $5.6 \,(+1.9/-1.0)$ kpc, pro-

viding a unique way to estimate the inclination i of a nearly spherical object once the distance D is known. The corrected mean velocity fields are consistent with regular rotation, and the mean velocity dispersions display significant deviations from isotropy.

We binned the individual measurements on the plane of the sky to search efficiently through the parameter space of the models. Tests on an analytic model demonstrated that our approach is capable of measuring the cluster distance to an accuracy of about 6 per cent. Application to ω Cen revealed no dynamical evidence for a significant radial dependence of the (V-band) stellar mass-to-light ratio M/L_V, in harmony with the relatively long relaxation time of the cluster. We found that our best-fit dynamical model has $M/L_V = 2.5 \pm 0.1$ $\mathrm{M_\odot/L_\odot}$ and $i = 50° \pm 4°$, which corresponds to an average intrinsic axial ratio of 0.78 ± 0.03. The best-fit dynamical distance $D = 4.8 \pm 0.3$ kpc (distance modulus 13.75 ± 0.13 mag) is significantly larger than obtained by means of simple spherical or constant-anisotropy axisymmetric dynamical models, and is consistent with the canonical value 5.0 ± 0.2 kpc obtained by photometric methods. The total mass of the cluster is $(2.5 \pm 0.3) \times 10^6$ $\mathrm{M_\odot}$.

Schwarzschild's approach also provides an insight into the intrinsic orbital structure of the cluster. Our best-fit model implies that ω Cen is close to isotropic inside a radius of about 10 arcmin and becomes increasingly tangentially anisotropic in the outer region, which displays significant mean rotation. We found that this may well be caused by the effects of the tidal field of the Milky Way. Furthermore, the best-fit model contains a separate disk-like component between 1 and 3 arcmin, contributing about 4% to the total mass. This phase-space structure, which might be linked to the multiple stellar populations observed in ω Cen, is expected to provide important constraints on its formation history.

We might improve our best-fit dynamical model of ω Cen and better constrain the distance and the other parameters, by extending the data-set with e.g. proper motions derived from HST images. Whereas with the ground-based proper motions we were unable to probe the center of ω Cen due to crowding, the high spatial resolution and high sensitivity of HST, results in many proper motion measurements in the very center, which allows the investigation of a possible central mass concentration in ω Cen.

We may also increase the kinematic constraints on our dynamical models by including mean correlated and higher-order velocity moments. With the parameter range considerably constrained, it now becomes also feasible to use non-linear maximum likelihood techniques to directly incorporate the discrete kinematic measurements. These techniques not only allow correlated and higher-order velocity moments to be included in a straightforward way, but also provide a natural way to incorporate measurements of age and metallicity indicators of individual stars in addition to their photometry and kinematics. By fitting an orbit-based model simultaneously to all these observations, different stellar populations can be separated in phase-space, after which their structure and dynamics can be studied separately.

We have shown that with the method described in this paper, we were able to measure the global parameters of ω Cen, including its distance, and investigate its intrinsic orbital structure. This method can also be applied to study other globular clusters and stellar clusters in the Milky Way, provided that accurate velocity measurements are available. With the amount of (photometric and kinematic) data quickly increasing, we expect this method to become an important tool to model these stellar systems and gain insight in their formation and evolution.

REFERENCES

Andrews D. F., Bickel P. J., Hampel F. R., Rogers W., Tukey J., 1972, Robust Estimates of Locations: Survey and Advances. Princeton University, Princeton

Bedin L. R., Piotto G., Anderson J., Cassisi S., King I. R., Momany Y., Carraro G., 2004, ApJ, 605, L125

Beers T. C., Flynn K., Gebhardt K., 1990, AJ, 100, 32

Benedict G. F., et al. 2002, AJ, 123, 473

Binney J., Tremaine S., 1987, Galactic Dynamics. Princeton, NJ, Princeton University Press

Binney J. J., Davies R. L., Illingworth G. D., 1990, ApJ, 361, 78

Cappellari M., 2002, MNRAS, 333, 400

Cappellari M., et al. 2004, in Carnegie Centennial Symposium I: Co-evolution of Black Holes and Galaxies, ed. L. Ho

Cappellari M., Verolme E. K., van der Marel R. P., Kleijn G. A. V., Illingworth G. D., Franx M., Carollo C. M., de Zeeuw P. T., 2002, ApJ, 578, 787

Carraro G., Lia C., 2000, A&A, 357, 977

Cretton N., de Zeeuw P. T., van der Marel R. P., Rix H., 1999, ApJS, 124, 383

Cudworth K. M., 1979, AJ, 84, 1312

Da Costa G. S., 1979, AJ, 84, 505

Davies R. L., Efstathiou G., Fall S. M., Illingworth G., Schechter P. L., 1983, ApJ, 266, 41

Dejonghe H., 1989, ApJ, 343, 113

Dickens R. J., Woolley R. v. d. R., 1967, Royal Greenwich Observatory Bulletin, 128, 255

Dinescu D. I., Girard T. M., van Altena W. F., 1999, AJ, 117, 1792

Dull J. D., Cohn H. N., Lugger P. M., Murphy B. W., Seitzer P. O., Callanan P. J., Rutten R. G. M., Charles P. A., 1997, ApJ, 481, 267

Emsellem E., Monnet G., Bacon R., 1994, A&A, 285, 723

Evans N. W., 1994, MNRAS, 267, 333

Evans N. W., de Zeeuw P. T., 1994, MNRAS, 271, oc202

Feast M. W., Thackeray A. D., Wesselink A. J., 1961, MNRAS, 122, 433

Ferraro F. R., Bellazzini M., Pancino E., 2002, ApJ, 573, L95

Freeman K. C., 1993, in ASP Conf. Ser. 48, eds. G. H. Smith, J. P. Brodie, p. 608

Freeman K. C., 2002, in ASP Conf. Ser. 265, eds. F. van Leeuwen, J. D. Hughes, G. Piotto, p. 423

Freeman K. C., Rodgers A. W., 1975, ApJ, 201, L71

Gascoigne S. C. B., Burr E. J., 1956, MNRAS, 116, 570

Gebhardt K., et al. 2003, ApJ, 583, 92

Gerhard O. E., 1993, MNRAS, 265, 213

Geyer E. H., Nelles B., Hopp U., 1983, A&A, 125, 359

Harris W. E., 1996, AJ, 112, 1487

Høg E., et al. 2000, VizieR Online Data Catalog, 1259, 0

Icke V., Alcaino G., 1988, A&A, 204, 115

Kalnajs A. J., 1999, in ASP Conf. Ser. 165, eds. B. K. Gibson, T. S. Axelrod, M. E. Putman, p. 325

Kenney J. F., Keeping E. S., 1951, The Distribution of the Standard Deviation. § 7.8 in *Mathematics of Statistics*, Pt. 2, 2nd ed. Princeton, NJ: Van Nostrand

King I. R., Anderson J., 2002, in ASP Conf. Ser. 265, eds. F. van Leeuwen, J. D. Hughes, G. Piotto, p. 21

King I. R., Hedemann E. J., Hodge S. M., White R. E., 1968, AJ, 73, 456

Kleyna J., Wilkinson M. I., Evans N. W., Gilmore G., Frayn C., 2002, MNRAS, 330, 792

Krajnović D., Cappellari M., Emsellem E., McDermid R. M., de Zeeuw P. T., 2005, MNRAS, 357, 1113

Lawson C. L., Hanson R. J., 1974, Solving least squares problems. Prentice-Hall Series in Automatic Computation, Englewood Cliffs: Prentice-Hall, 1974

Lee Y.-W., Joo J.-M., Sohn Y.-J., Rey S.-C., Lee H.-C., Walker A. R., 1999, Nature, 402, 55

Lee Y.-W., Rey S.-C., Ree C. H., Joo J.-M., Sohn Y.-J., Yoon S.-J., 2002, in ASP Conf. Ser. 265, eds. F. van Leeuwen, J. D. Hughes, G. Piotto, p. 305

Lub J., 2002, in ASP Conf. Ser. 265, eds. F. van Leeuwen, J. D. Hughes, G. Piotto, p. 95

Lucy L. B., 1974, AJ, 79, 745

Mandushev G., Staneva A., Spasova N., 1991, A&A, 252, 94

Martin W. C., 1938, Annalen van de Sterrewacht te Leiden, 17, 1

Mayor M., et al. 1996, in ASP Conf. Ser. 90, eds. E. F. Milone, J.-C. Mermilliod, p. 190

Mayor M., et al. 1997, AJ, 114, 1087 [M97]

McNamara B. J., Harrison T. E., Baumgardt H., 2004, ApJ, 602, 264

Merrifield M. R., Kent S. M., 1990, AJ, 99, 1548

Merritt D., 1993, ApJ, 413, 79

Merritt D., 1997, AJ, 114, 228

Merritt D., Meylan G., Mayor M., 1997, AJ, 114, 1074

Merritt D., Saha P., 1993, ApJ, 409, 75

Meylan G., 1987, A&A, 184, 144

Meylan G., Mayor M., Duquennoy A., Dubath P., 1995, A&A, 303, 761

Monnet G., Bacon R., Emsellem E., 1992, A&A, 253, 366

Norris J. E., Freeman K. C., Mayor M., Seitzer P., 1997, ApJ, 487, L187

Pancino E., Ferraro F. R., Bellazzini M., Piotto G., Zoccali M., 2000, ApJ, 534, L83

Pancino E., Seleznev A., Ferraro F. R., Bellazzini M., Piotto G., 2003, MNRAS, 345, 683

Perryman M. A. C., ESA 1997, The HIPPARCOS and TYCHO catalogues. ESA SP 1200

Peterson R. C., Cudworth K. M., 1994, ApJ, 420, 612

Peterson R. C., Rees R. F., Cudworth K. M., 1995, ApJ, 443, 124

Platais I., Wyse R. F. G., Hebb L., Lee Y., Rey S., 2003, ApJ, 591, L127

Press W. H., Teukolsky S. A., Vettering W. T., Flannery B. P., 1992, Numerical Recipes. Cambridge Univ. Press, Cambridge

Rees R. F., 1997, in ASP Conf. Ser. 127, ed. R. M. Humphreys, p. 109

Reijns R. A., Seitzer P., Arnold R., Freeman K. C., Ingerson T., van den Bosch R. C. E., van de Ven G., de Zeeuw P. T., 2005, A&A, pp in press, astro–ph/0509227 [Paper II]

Richstone D. O., Tremaine S., 1988, ApJ, 327, 82

Rix H., de Zeeuw P. T., Cretton N., van der Marel R. P., Carollo C. M., 1997, ApJ, 488, 702

Romanowsky A. J., Kochanek C. S., 2001, ApJ, 553, 722

Satoh C., 1980, PASJ, 32, 41

Scarpa R., Marconi G., Gilmozzi R., 2003, A&A, 405, L15

Schwarzschild M., 1979, ApJ, 232, 236

Schwarzschild M., 1982, ApJ, 263, 599

Schwarzschild M., 1993, ApJ, 409, 563

Seitzer P. O., 1983, Ph.D. Thesis, Australian National Univ.

Spitzer L. J., Hart M. H., 1971, ApJ, 164, 399

Stetson P. B., 1993, in IAU Colloq. 136, eds. C. J. Butler, I. Elliott, p. 291

Suntzeff N. B., Kraft R. P., 1996, AJ, 111, 1913 [SK96]

Thompson I. B., Kaluzny J., Pych W., Burley G., Krzeminski W., Paczyński B., Persson S. E., Preston G. W., 2001, AJ, 121, 3089

Toomre A., Toomre J., 1972, ApJ, 178, 623

Trager S. C., King I. R., Djorgovski S., 1995, AJ, 109, 218

Tremaine S., et al. 2002, ApJ, 574, 740

Tsuchiya T., Korchagin V. I., Dinescu D. I., 2004, MNRAS, 350, 1141

van den Bosch R. C. E., de Zeeuw P. T., Gebhardt K., Noyola E., van de Ven G., 2005, ApJ, submitted

van der Marel R. P., 2004, in Carnegie Centennial Symposium I: Co-evolution of Black Holes and Galaxies, ed. L. Ho, p. 37

van der Marel R. P., Cretton N., de Zeeuw P. T., Rix H., 1998, ApJ, 493, 613

van der Marel R. P., Franx M., 1993, ApJ, 407, 525

van Leeuwen F., Hughes J. D., Piotto G., eds, 2002, Omega Centauri, A Unique Window into Astrophysics, ASP Conf. Ser. 265

van Leeuwen F., Le Poole R. S., 2002, in ASP Conf. Ser. 265, eds. F. van Leeuwen, J. D. Hughes, G. Piotto, p. 41

van Leeuwen F., Le Poole R. S., Reijns R. A., Freeman K. C., de Zeeuw P. T., 2000, A&A, 360, 472 [Paper I]

Vandervoort P. O., 1984, ApJ, 287, 475

Vasilevskis S., van Leeuwen F., Nicholson W., Murray C. A., 1979, A&AS, 37, 333

Verolme E. K., de Zeeuw P. T., 2002, MNRAS, 331, 959

Verolme E. K., et al. 2002, MNRAS, 335, 517

White R. E., Shawl S. J., 1987, ApJ, 317, 246

Woolley R. v. d. R., 1966, Royal Observatory Annals, 2, 1

Appendix A   Maximum likelihood estimation velocity moments

We use the average kinematics of stars that fall within apertures on the plane of the sky. This is comparable to the kinematics from the integrated spectra of galaxies in an aperture. A very important difference is, however, that we have to take into account the errors on the individual velocity measurements.

A possible way to measure the mean velocity and velocity dispersion, is to fit a Gaussian distribution to the velocity histogram of the stars that fall within an aperture. Whereas the mean velocity V is well estimated, the best-fit mean velocity dispersion σ_{fit} is too large, as the Gaussian distribution is broadened due to the velocity errors. This additional 'instrumental' dispersion σ_{ins} can be estimated by the mean of the velocity errors. The corrected mean velocity dispersion σ then follows from $\sigma^2 = \sigma_{\mathrm{fit}}^2 - \sigma_{\mathrm{ins}}^2$. Since this is only an approximate correction, we use a maximum likelihood estimate of the velocity moments that at the same time corrects for each individual velocity error.

Suppose $\mathcal{L}(v)$ is the (intrinsic) velocity distribution of the stars in an aperture, in one of the three principal directions. We can consider each stellar velocity measurement v_i in that aperture as drawn from this distribution, or alternatively, the product of $\mathcal{L}(v)$ with a delta function around v_i, integrated over all velocities. Due to (instrumental) uncertainties this delta-function is broadened, and we assume that it can

be described by a Gaussian around v_i, with the corresponding velocity error σ_i as the standard deviation. For a sufficient number of draws N, i.e. velocity measurements in the aperture, we can then recover the (unknown) velocity distribution $\mathcal{L}(v)$ by maximizing the likelihood

$$L(V, \sigma, \dots) = \prod_{i=1}^{N} \int_{-\infty}^{\infty} \mathcal{L}(v) \frac{e^{-\frac{1}{2}\left(\frac{v_i - v}{\sigma_i}\right)^2}}{\sqrt{2\pi}\sigma_i} \, \mathrm{d}v, \tag{A.1}$$

or, equivalently, minimizing $\Lambda \equiv -2\ln(L)$, with respect to the mean velocity V, mean velocity dispersion σ and possible higher-order velocity moments.

It is possible to recover $\mathcal{L}(v)$ in a non-parametric way using (extensions of) Lucy's (1974) method, but exploiting the fact that Gaussians are good low-order approximations, the velocity distribution is often parameterized by a Gauss-Hermite (GH) series (van der Marel & Franx, 1993; Gerhard, 1993). It has the advantage that it only requires the storage of the velocity moments (V, σ, h_3, h_4, ...) instead of the full velocity distribution. Furthermore, it allows a simple velocity scaling of the model, which is useful when investigating the effect of a change in the stellar mass-to-light ratio.

Another advantage of parameterizing $\mathcal{L}(v)$ comes from the observation that the integral in (A.1) is the *convolution* of the velocity distribution and the Gaussian of each velocity measurement. For a Gaussian velocity distribution this convolution is straightforward, but also in the case that $\mathcal{L}(v)$ is described by a GH series, the convolution can be carried out analytically. This makes it feasible to apply the method to a large number of discrete measurements and to estimate the uncertainties on the extracted velocity moments by means of the Monte Carlo bootstrap method (§ 15.6 of Press et al. 1992).

In the case of no measurement errors, the maximum likelihood estimator of the standard deviation σ, given by

$$\hat{\sigma} = \sqrt{\frac{1}{n}\sum_{i=1}^{n}(v_i - \overline{v})^2}, \qquad \text{with } \overline{v} = \sum_{i=1}^{n} v_i, \tag{A.2}$$

is a biased estimator, underestimating the true σ by a factor (see also e.g. Kenney & Keeping 1951, p. 171)

$$b(n) = \sqrt{\frac{2}{n}}\frac{\Gamma\left(\frac{n}{2}\right)}{\Gamma\left(\frac{n-1}{2}\right)} = 1 - \frac{3}{4n} - \frac{7}{32n^2} - \dots. \tag{A.3}$$

where Γ is the gamma function. When we consider the measurement errors σ_i, there is no such simple analytical bias correction as (A.3). However, we can use the latter result to derive the following approximate corrected standard deviation estimator

$$\tilde{\sigma} \approx \frac{1}{b(n)}\sqrt{\hat{\sigma}^2 + [1 - b^2(n)]\,\overline{\sigma^2}}, \tag{A.4}$$

where $\hat{\sigma}$ is the maximum likelihood estimated dispersion and $\overline{\sigma^2} = \frac{1}{n}\sum_{i=1}^{n}\sigma_i^2$ the average measurement error.

APPENDIX B   POLAR GRID OF APERTURES

We use Monte Carlo simulations of the observed stellar velocities and corresponding errors to investigate the recovery of their average kinematics. We mimic the stellar velocity observations by randomly drawing from an assumed intrinsic Gaussian velocity distribution, with given mean velocity V_0 and velocity dispersion σ_0. This set of intrinsic velocities, is then 'instrumentally' broadened by adding to each velocity a random drawing from a Gaussian with zero mean and the velocity error as standard deviation. These velocity errors are simulated by randomly drawing from the observed velocity error distribution (right panels of Fig. 5). For the latter we use the *rejection method* (§ 7.3 of Press et al. 1992), with a Lorentzian distribution as comparison function. In this way, we create, for a given number of stars, 500 sets of simulated velocities and corresponding errors.

Next, we use the maximum likelihood method of Appendix A to calculate the mean velocity and velocity dispersion for each simulated set separately. In Fig. B.1, we compare the (biweight[10]) mean (filled circles) of these 500 mean velocity and velocity dispersion measurements with V_0 and σ_0 (horizontal lines) of the given intrinsic Gaussian velocity distribution. The error bars are the (biweight) standard deviation of the kinematic measurements, and indicate the precision with which the kinematics can be measured, given the observed velocity error distribution. The precision increases with increasing number of stars per bin. The precision also increases with decreasing intrinsic mean velocity dispersion σ_0. To remove the latter dependency, we give *relative* kinematic measurements and corresponding errors, i.e., divided by the (arbitrarily) chosen value for σ_0.

Both the mean velocity and velocity dispersion are recovered well. To obtain a better precision, we can increase the number of stars per aperture, but at the same time the spatial resolution decreases, as we have to increase the size of the apertures. We find that between 50 and 100 stars per aperture is a good compromise. For the proper motions this implies a (relative) precision for the mean velocity V and velocity dispersion σ of respectively $\Delta V/\sigma \sim 0.12$ and $\Delta\sigma/\sigma \sim 0.09$. For the line-of-sight velocities we find similar values, respectively $\Delta V/\sigma \sim 0.12$ and $\Delta\sigma/\sigma \sim 0.08$.

Given the average proper motion dispersion of about 0.5 mas yr^{-1} for ω Cen (§ 7.2), this means we expect to measure the mean proper motion and dispersions with an average (absolute) precision of respectively 0.06 mas yr^{-1} and 0.05 mas yr^{-1}. Similarly, with an average line-of-sight velocity dispersion of about 14 km s^{-1} for ω Cen, we expect to measure the mean line-of-sight velocity and dispersion with an average precision of respectively 1.7 km s^{-1} and 1.1 km s^{-1}.

Indeed, the average of the uncertainties in the kinematics given in Table 3 and 4 are consistent with these expectations. Moreover, as predicted, the decrease in the uncertainties with radius is proportional to the decrease in dispersion. In other words, if we divide the uncertainties by the corresponding dispersions, we find nearly constant (relative) precisions, $\Delta V/\sigma \sim 0.11$ and $\Delta\sigma/\sigma \sim 0.08$ for both proper motions and line-of-sight velocities, consistent with the above simulated precisions.

To enhance the signal-to-noise of the observations, we first reflect all measurements back to the first quadrant ($x' \geq 0$, $y' \geq 0$). We exploit the fact that for an axisym-

---

[10]The biweight mean and biweight standard deviation (e.g., Andrews et al. 1972; Beers, Flynn & Gebhardt 1990) are robust estimators for a broad range of non-Gaussian underlying populations and are less sensitive to outliers than other moment estimators.
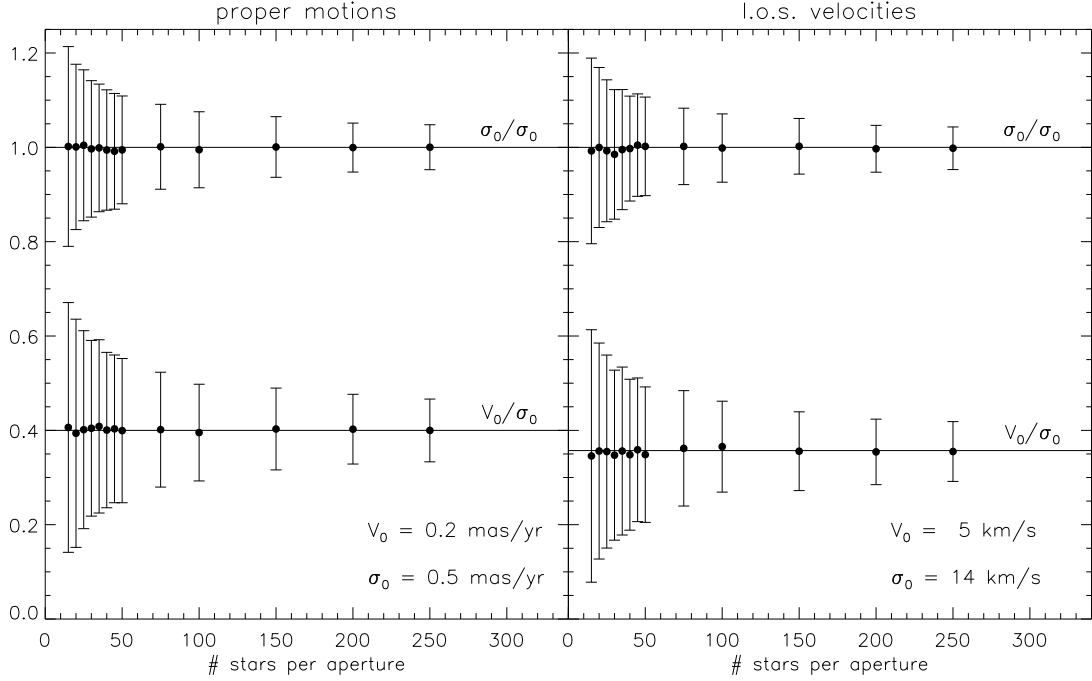
FIGURE B.1 — *Recovery of maximum-likelihood-estimated kinematics from proper motions (left panel) and line-of-sight velocities (right panel). For a given number of stars per aperture, velocities and corresponding errors are simulated by randomly drawing from an intrinsic Gaussian distribution with mean velocity V_0 and velocity dispersion σ_0, broadened by velocity errors randomly drawn from the observed velocity error distributions (left panels Fig. 5). Each filled circle with error bar shows the mean and standard deviation of the measured kinematics from 500 such simulations. As a compromise between lower precision (larger error bars) for a small number of stars per aperture, and lower spatial resolution (larger bins) for a larger number of stars, we choose to have between 50 and 100 stars per bin.*

metric object, the proper motions in the x'-direction are symmetric in the projected minor axis, while the proper motions in the y'-direction as well as the line-of-sight velocities are symmetric in the projected major axis. Since our models are intrinsically axisymmetric, it is equivalent to fit either to the original or to the reflected data.

We use a polar grid of apertures on (the first quadrant of) the plane of the sky to better approximate the shape of photometric and kinematic observations. Every aperture is characterized by its central radius $r_0 > 0$ and angle $0° < \theta_0 < 90°$, together with its radial and angular width, denoted by Δr and $\Delta\theta$, respectively. We construct the polar grids such that each aperture has (at least) 50 stars, together with the requirement that the apertures are as 'round' as possible in the sense that $\Delta r \approx r_0 \Delta\theta$. The latter avoids (very) radial or angular elongated apertures, which would include stars from (very) different positions, with probably different (kinematical) properties than the stars near the center of the aperture.

APPENDIX C   SIMPLE DISTANCE ESTIMATE

The most straightforward way to obtain a dynamical distance estimate is from the ratio of the line-of-sight velocity dispersion σ_{los} and the proper motion velocity dispersion σ_{pm} for spherically symmetric objects (e.g., Binney & Tremaine 1987, p. 280)

$$D \ (\mathrm{kpc}) = \frac{\sigma_{\mathrm{los}} \ (\mathrm{km\,s^{-1}})}{4.74 \, \sigma_{\mathrm{pm}} \ (\mathrm{mas\,yr^{-1}})}. \tag{C.1}$$

Using, from the 2295 selected stars with proper motions and 2163 selected stars with line-of-sight velocities, the 718 stars for which all three velocity components are measured, we find for the two mean proper motion dispersion components $\sigma_{x'} = 0.58 \pm 0.02$ mas yr^{-1} and $\sigma_{y'} = 0.55 \pm 0.02$ mas yr^{-1}, and for the mean line-of-sight velocity dispersion $\sigma_{z'} = 12.3 \pm 0.3$ km s^{-1}. Substituting the latter value together with the average proper motion dispersion in (C.1), we obtain a distance of $D = 4.6 \pm 0.2$ kpc.

This value is below the canonical distance $D = 5.0 \pm 0.2$ (Harris et al. 1996). The above simple distance estimate is not valid for ω Cen, which is not spherically symmetric. Moreover, although the above average values for $\sigma_{x'}$ and $\sigma_{y'}$ are just consistent with each other, from the left panel of Fig. C.1 it is clear that the profile of the mean proper motion dispersion profile of $\sigma_{x'}$ (dotted) lies systematically above that of $\sigma_{y'}$ (dashed). A non-spherical anisotropic model is needed to explain these observations. Here we consider a simple model with constant anisotropy.

If we make the (ad-hoc) assumption that the velocity ellipsoid is oblate with intrinsic semi-axis lengths $\sigma_x = \sigma_y \equiv \sigma$ and $\sigma_z = q_{\mathrm{ve}} \sigma$ (all in km s^{-1}), where q_{ve} is the average intrinsic flattening, the observed velocity dispersions are given by

$$\begin{aligned} \sigma_{x'} &= \sigma \, / \, 4.74 \, D \quad \mathrm{mas\,yr^{-1}}, \\ \sigma_{y'} &= q'_{\mathrm{ve}} \, \sigma \, / \, 4.74 \, D \quad \mathrm{mas\,yr^{-1}}, \\ \sigma_{z'} &= \left[1 - (1 - q'^2_{\mathrm{ve}}) \cot^2 i \right]^{1/2} \sigma \quad \mathrm{km\,s^{-1}}, \end{aligned} \tag{C.2}$$

where we have used eq. (2.2) and the relation $q^2 \sin^2 i = q'^2 - \cos^2 i$. Using the best-fit value for $D \tan i$ of 5.6 kpc (§ 4.5), we eliminate the inclination i. Next, by fitting the ratios of the line-of-sight velocity dispersion over the proper motion dispersion components, $\sigma_{z'}/\sigma_{x'}$ and $\sigma_{z'}/\sigma_{y'}$, to the observations in the left panel of Fig. 8, we determine the best-fit values for the remaining two free parameters: the distance D and the (projected) flattening of the velocity ellipsoid q'_{ve}.

Since we use the full dispersion profiles and we allow for an anisotropic velocity distribution, this simple way to obtain a dynamical distance estimate goes beyond the above spherical symmetric approach. If $q'_{\mathrm{ve}} = 1$ in eq. (C.2), we recover this approach in which both ratios are equal and the distance follows from eq. (C.1).

We show in the right panel of Fig. C.1 the $\Delta\chi^2$ contours for a range of q'_{ve} and D. The overall minimum, indicated by a cross, corresponds to the best-fit values $q'_{\mathrm{ve}} = 0.92 \pm 0.05$ and $D = 4.54 \pm 0.14$ kpc. The isotropic case ($q'_{\mathrm{ve}} = 1$) is excluded at about the 95.4%-level. The best-fit (projected) flattening of the velocity ellipsoid is less than the average observed flattening $q' = 0.879 \pm 0.007$ (hashed region) from the stellar photometry of ω Cen (Geyer et al. 1983), although an equivalent value is not excluded (at the 68.3%-level). The velocity distribution is expected to be less flattened, since it traces more directly the potential, which in general is rounder than the light distribution (see e.g. p. 48 of Binney & Tremaine 1987).
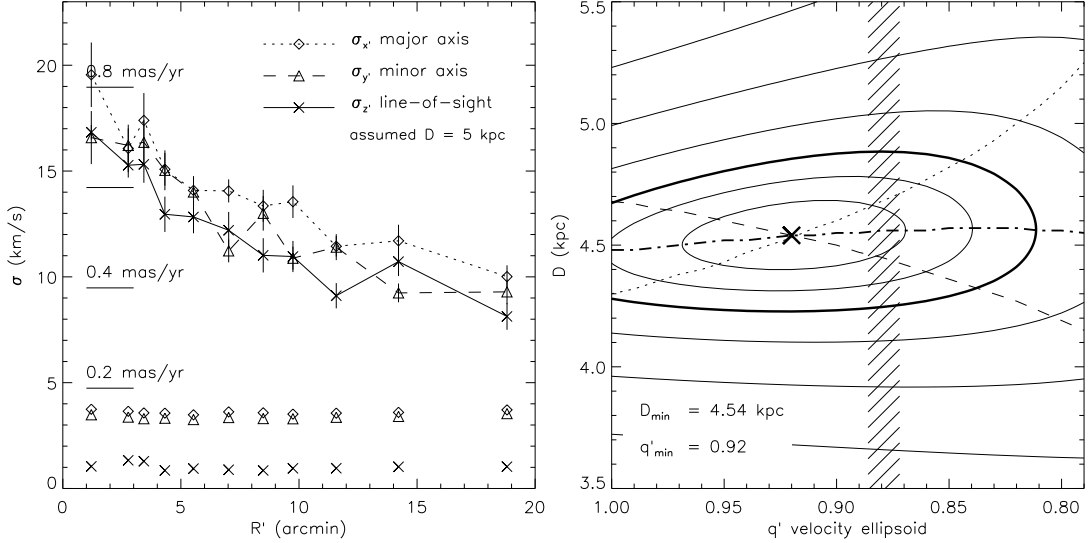
FigURE C.1 — *Left panel: velocity dispersion profiles calculated along concentric rings. Assuming the canonical distance of 5 kpc, the profiles of the proper motion components in the x'-direction (dotted curve with diamonds) and y'-direction (dashed curve with triangles) are converted into the same units of $\mathrm{km\,s^{-1}}$ as the line-of-sight profile in the z'-direction (solid curve with crosses). The black horizontal lines indicate the corresponding scale in $\mathrm{mas\,yr^{-1}}$. Below the profiles, the mean velocity error per ring is indicated by the corresponding symbols. Right panel: Assuming an oblate velocity ellipsoid with constant (projected) flattening, the ratio of the line-of-sight over the proper motion velocity dispersion profiles yields an estimate for the dynamical distance D. The best-fit values correspond to the minimum (cross) in the $\Delta\chi^2$ contour plot, where the inner three contours are drawn at the 68.3%, 95.4% and 99.7% (thick contour) levels, and subsequent contours correspond to a factor of two increase in $\Delta\chi^2$. For increasing flattening of the velocity ellipsoid, starting with the isotropic case on the left axis, the dotted (dashed) curve shows the corresponding best-fit distance if only the profile of the proper motion in the x'-direction (y'-direction) is used, and the dotted-dashed curve if both are used. The observed flattening from the stellar photometry (Geyer et al. 1983) is indicated by the hashed region.*

If we only fit the ratio $\sigma_{z'}/\sigma_{x'}$, the dotted curve shows the best-fit distance at given flattening. While in this case the distance increases with flattening, almost exactly the opposite happens if we only fit the ratio $\sigma_{z'}/\sigma_{y'}$ (dashed curve). Simultaneously fitting both ratios does not provide a good fit (the χ^2 value is larger than the number of degrees of the freedom) and the resulting best-fit distance (dotted-dashed curve) of about 4.5 kpc is significantly below the canonical distance of 5.0 kpc.

We conclude that both the simple distance estimate (C.1) and the above constant-anisotropy axisymmetric model are not valid for ω Cen and underestimate its distance. To explain the observed kinematics of ω Cen and obtain a reliable distance estimate, one needs a non-spherical dynamical model with varying anisotropy, like the Schwarzschild modeling technique used here.